



Article

# Enhancing Methylene Blue Removal through Adsorption and Photocatalysis—A Study on the GO/ZnTiO<sub>3</sub>/TiO<sub>2</sub> Composite

Ximena Jaramillo-Fierro <sup>1,\*</sup> and Guisella Cuenca <sup>2</sup>

<sup>1</sup> Departamento de Química, Facultad de Ciencias Exactas y Naturales, Universidad Técnica Particular de Loja, San Cayetano Alto, Loja 1101608, Ecuador

<sup>2</sup> Ingeniería Química, Facultad de Ciencias Exactas y Naturales, Universidad Técnica Particular de Loja, San Cayetano Alto, Loja 1101608, Ecuador; gpcuenca0@utpl.edu.ec

\* Correspondence: xvjaramillo@utpl.edu.ec; Tel.: +593-7-3701444

**Abstract:** This study focuses on synthesizing and characterizing a graphene oxide/ZnTiO<sub>3</sub>/TiO<sub>2</sub> (GO/ZTO/TO) composite to efficiently remove methylene blue (MB) from water, presenting a novel solution to address industrial dye pollution. GO and ZTO/TO were synthesized by the modified Hummers and sol-gel methods, respectively, while GO/ZTO/TO was prepared using a hydrothermal process. The structural and surface properties of the composite were characterized using various analytical techniques confirming the integration of the constituent materials and suitability for dye adsorption. The study revealed that GO/ZTO/TO exhibits an adsorption capacity of 78 mg g<sup>-1</sup> for MB, with only a 15% reduction in adsorption efficiency until the fifth reuse cycle. Furthermore, the study suggests optimal adsorption near neutral pH and enhanced performance at elevated temperatures, indicating an endothermic reaction. The adsorption behavior fits the Langmuir isotherm, implying monolayer adsorption on homogeneous surfaces, and follows pseudo-second-order kinetics, highlighting chemical interactions at the surface as the rate-limiting step. The photocatalytic degradation of MB by GO/ZTO/TO follows pseudo-first-order kinetics, with a higher rate constant than that of GO alone, demonstrating the enhanced photocatalytic activity of the composite. In conclusion, GO/ZTO/TO emerges as a promising and sustainable approach for water purification, through an adsorption process and subsequent photocatalytic degradation.



**Citation:** Jaramillo-Fierro, X.; Cuenca, G. Enhancing Methylene Blue Removal through Adsorption and Photocatalysis—A Study on the GO/ZnTiO<sub>3</sub>/TiO<sub>2</sub> Composite. *Int. J. Mol. Sci.* **2024**, *25*, 4367. <https://doi.org/10.3390/ijms25084367>

Academic Editor: Meysam Tayebi

Received: 29 March 2024

Revised: 10 April 2024

Accepted: 11 April 2024

Published: 15 April 2024



**Copyright:** © 2024 by the authors. Licensee MDPI, Basel, Switzerland. This article is an open access article distributed under the terms and conditions of the Creative Commons Attribution (CC BY) license (<https://creativecommons.org/licenses/by/4.0/>).

**Keywords:** graphene oxide; ZnTiO<sub>3</sub>/TiO<sub>2</sub>; adsorption; photocatalysis; methylene blue; water purification

## 1. Introduction

Industrial dye pollution is a severe environmental issue stemming from the widespread use of synthetic dyes across various sectors such as textiles, leather, paper, and plastics. The textile industry alone discharges approximately 146,000 tons of dyes into the environment annually through wastewater [1]. This substantial effluent generation occurs because dyeing processes in the textile industry experience a dye loss of 10% to 25%, with 2% to 20% of these dyes ending up as liquid waste in natural water bodies. Wastewater from these processes contains dye concentrations ranging from 10 to 200 mg L<sup>-1</sup>, leading to a significant dispersion of dyes in aquatic environments [2,3]. This dispersion adversely affects water clarity, harms aquatic life by obstructing their oxygen supply, and poses risks to human health [4]. The detrimental effects are largely due to the toxic, mutagenic, and carcinogenic properties of many dyes, attributed to the presence of aromatic entities like benzidine and naphthalene [5]. Specifically, methylene blue, predominantly used in textile applications, poses a considerable risk to aquatic ecosystems due to its toxicity and persistence in nature [6,7]. Given the global increase in synthetic dye production and the expansion of industries that utilize these colorants, addressing industrial dye pollution has become imperative for environmental protection and sustainability.

Efforts to extract methylene blue and similar dyes from aquatic habitats have introduced a range of physicochemical and biological approaches [8]. These remedial strategies encompass physical methods such as ion exchange [9], membrane filtration [10], and adsorption [11], chemical processes including ozonation [12], the oxidation process [13], ultrasound [14], and photocatalysis [15], and aerobic and anaerobic biological treatments [16].

In particular, adsorption is favored for its affordability, facile application, effectiveness, and the possibility of enhancement through technological innovations and the development of new materials [17,18]. This technique depends on the electrostatic attraction between pollutants and the surface of the adsorbent, through mechanisms like electrostatic forces, hydrogen bonds, and  $\pi$ - $\pi$  interactions [19]. Alternatively, heterogeneous photocatalysis, recognized as an advanced oxidation process, facilitates the thorough mineralization of pollutants via a series of redox reactions initiated by the photoactivation of the catalyst under either natural or artificial illumination [20].

The performance of adsorption and photodegradation is influenced by the characteristics of the materials and operational conditions [21]. Studying these factors is essential for designing efficient materials and methods for specific pollutant removal. Ideal materials for these processes should exhibit a vast surface area, numerous active sites, chemical stability, high adsorption and oxidation capacities, non-toxicity, environmental friendliness, efficiency, cost-effectiveness, regenerability, and accessibility [22].

Explorations for potent dye-removing materials, including for the removal of methylene blue (MB) from water, have ventured into activated carbon, zeolites, clays, metal oxides, polymers, and graphene and its derivatives among others [23–26]. Graphene, distinguished by a two-dimensional hexagonal carbon atom arrangement, showcases exceptional electrical and thermal conductivities, which bolster its contaminant adsorption capabilities. Its vast hydrophobic surface and specific surface area render it an effective adsorbent [27,28]. Graphene oxide (GO), derived from graphene via oxidation, introduces functional groups that boost adsorption through chemical bonds [29–33]. Reduced graphene oxide (rGO), obtained by reducing GO, partially reinstates the structure of graphene and adsorption features [34,35].

The literature indicates that incorporating dopant elements into graphene, such as boron (B), nitrogen (N), sulfur (S), and phosphorus (P), significantly alters its electronic interaction with various molecules, enhancing its selectivity and adsorption capacity. Particularly, nitrogen doping introduces active sites and defects into the graphene structure, expanding its adsorption capacity toward organic compounds in aqueous solutions [36,37]. Additionally, the integration of bimetallic frameworks, such as iron and cobalt alloys (FeCo) or combinations of zinc and nickel (ZnNi), notably improves the catalytic and photocatalytic activity of the compounds, promoting the generation of reactive oxygen species and optimizing the decomposition of organic compounds under visible light. These bimetallic systems leverage the synergy between metals for greater charge separation and generation of reactive species, offering advanced pathways for the efficient adsorption and catalysis of persistent organic pollutants [38,39].

Recent attention has focused on graphene-based materials for water purification, taking advantage of their extensive surface area and porosity for the efficient capture of dye molecules, including methylene blue, achieving removal rates exceeding 95% [40–42]. Prior investigations have delved into the structural attributes of graphene (G), graphene oxide (GO), and related derivatives, elucidating their molecular adsorption properties [43–45]. Concurrently, ZnTiO<sub>3</sub>, a mixed oxide produced via the sol-gel method during ZnO-TiO<sub>2</sub> coupling, has been thoroughly explored for its numerous applications. This polar oxide is formed by Ti<sup>4+</sup> (3d<sup>0</sup>) and Zn<sup>2+</sup> (3d<sup>10</sup>), which present a strong Coulombic repulsion between themselves [46,47], which allows the use of ZnTiO<sub>3</sub> as a material with ferroelectric, nonlinear optical and piezoelectric properties, and as a photocatalyst in environmental remediation processes [48–51]. ZnTiO<sub>3</sub> is often synthesized with impurities such as anatase and rutile, resulting in the mixed oxide ZnTiO<sub>3</sub>/TiO<sub>2</sub>. This mixed oxide has been the target of several investigations, due to its physicochemical properties, versatility, low cost,

and respect for the environment. Indeed, previous studies have thoroughly explored its applications as an adsorbent and photocatalyst, particularly for removing methylene blue dye from water [52–54].

Although there are numerous studies on the properties of graphene oxide (GO) and the semiconductors ZnTiO<sub>3</sub> and TiO<sub>2</sub>, there is not enough information on the adsorbent and photocatalytic capabilities of their combined compound, GO/ZnTiO<sub>3</sub>/TiO<sub>2</sub> (GO/ZTO/TO) and its efficiency in removing contaminants in aqueous systems. The novelty of this study lies in addressing this knowledge gap and exploring the effectiveness of the GO/ZTO/TO composite in the removal of MB through adsorption and photocatalysis processes. Focusing on critical variables such as solution pH, dye concentration, reaction temperature, and contact time, this work aims to clarify how these conditions influence the adsorption and photodegradation performance of the compound. Furthermore, the recyclability of the composite is evaluated, showing that it maintains a high MB removal capacity even after multiple use cycles, underscoring its sustainability and reducing the need for frequent material replacement. This research not only deepens the understanding of the mechanisms of MB removal by the GO/ZTO/TO composite but also highlights its advantages as an advanced adsorbent material, including its recyclability and the potential to optimize water purification and efficient removal of contaminants, marking a significant advance in wastewater treatment technologies.

## 2. Results

Table 1 lists the mathematical equations used in this study for the respective calculations.

**Table 1.** Summary of the mathematical equations used in this study for data analysis.

Denomination	Equation	Parameters
Scherrer equation	$D = \frac{\kappa\lambda}{\beta\cos\theta} \quad (1)$	D = Crystallite size (nm) λ = Wavelength of the X-ray beam (0.15406 nm) κ = Shape factor (0.89) θ = Bragg angle β = Full width at half peak height maximum (FWHM) of the X-ray diffraction peak
Adsorbate adsorbed	$q_e = (C_0 - C_e) \times \frac{v}{w} \quad (2)$	C <sub>0</sub> = Initial concentration (mg L <sup>-1</sup> ) C <sub>e</sub> = Equilibrium concentration (mg L <sup>-1</sup> ) w = Mass of the adsorbent (g) v = Volume of the solution (L)
Langmuir	$\frac{C_e}{q_e} = \frac{1}{K_L q_{max}} + \frac{C_e}{q_{max}} \quad (3)$	q <sub>max</sub> = Maximum monolayer adsorption (mg g <sup>-1</sup> ) K <sub>L</sub> = Equilibrium Langmuir constant related to the adsorption energy (L mg <sup>-1</sup> ) C <sub>e</sub> = Concentration of adsorbate in solution at equilibrium (mg L <sup>-1</sup> )
Freundlich	$q_e = K_F C_e^{\frac{1}{n}} \quad (4)$	K <sub>F</sub> = Freundlich constant (L mg <sup>-1</sup> ) 1/n = Adsorption intensity constant Note: For favorable adsorption, the value of n should be between 1 and 10
Temkin	$q_e = B \ln(AC_e) \quad (5)$	q <sub>e</sub> = Adsorbate adsorbed per unit weight (mg g <sup>-1</sup> ) at equilibrium A = Temkin isotherm constant (L g <sup>-1</sup> ) C <sub>e</sub> = Concentration of adsorbate in solution at equilibrium (mg L <sup>-1</sup> ) B = Constant related to the heat adsorption

Table 1. Cont.

Denomination	Equation	Parameters
Constant of heat adsorption	$B = \frac{RT}{b}$ (6)	b = Temkin constant (J mol <sup>-1</sup> ) T = Absolute temperature (K) R = Gas constant (8.314 J mol <sup>-1</sup> K <sup>-1</sup> )
Separation factor	$R_L = \frac{1}{(1+K_L C_e)}$ (7)	K <sub>L</sub> = Equilibrium Langmuir constant related to the adsorption energy (L mg <sup>-1</sup> ) C <sub>e</sub> = Concentration of adsorbate in solution at equilibrium (mg L <sup>-1</sup> ) Note: 0 < R <sub>L</sub> < 1, suitable adsorption, R <sub>L</sub> > 1 suitable adsorption, R <sub>L</sub> = 0 irreversible adsorption, R <sub>L</sub> = 1 linear adsorption.
Gibbs free energy	$\Delta G^0 = -RT \ln k_C$ (8)	ΔG <sup>0</sup> = Gibbs free energy (kJ mol <sup>-1</sup> ), ΔH <sup>0</sup> = Enthalpy (kJ mol <sup>-1</sup> ) ΔS <sup>0</sup> = Entropy (kJ mol <sup>-1</sup> K <sup>-1</sup> )
Van't Hoff equation	$\ln k_C = \frac{-\Delta H^0}{R} \times \frac{1}{T} + \frac{\Delta S^0}{R}$ (9)	k <sub>C</sub> = Dimensionless parameter T = Absolute temperature (K) R = Universal gas constant (8.314 J mol <sup>-1</sup> K <sup>-1</sup> )
	$k_C = k_L \times M_w \times 1000 \times 55.5$ (10)	k <sub>L</sub> = Langmuir constant (L mg <sup>-1</sup> ) M <sub>w</sub> = Adsorbate weight (g mol <sup>-1</sup> )
Pseudo-first-order	$\ln(q_e - q_t) = \ln(q_e) - k_1 t$ (11)	k <sub>1</sub> = Rate constant (min <sup>-1</sup> ) q <sub>e</sub> = Adsorbate adsorbed per unit weight (mg g <sup>-1</sup> ) at equilibrium q <sub>t</sub> = Adsorbate adsorbed per unit weight (mg g <sup>-1</sup> ) at any time (t)
Pseudo-second-order	$\frac{t}{q_t} = \frac{1}{k_2 q_e^2} + \frac{1}{q_e} t$ (12)	k <sub>2</sub> = Rate constant (g mg <sup>-1</sup> min <sup>-1</sup> ) q <sub>e</sub> = Adsorbate adsorbed per unit weight (mg g <sup>-1</sup> ) at equilibrium q <sub>t</sub> = Adsorbate adsorbed per unit weight (mg g <sup>-1</sup> ) at any time (t)
Elovich	$q_t = \frac{1}{\beta} \ln(\alpha\beta) + \frac{1}{\beta} \ln(t)$ (13)	q <sub>t</sub> = Adsorbate adsorbed per unit weight (mg g <sup>-1</sup> ) at any time (t) α = Constant related to chemisorption rate β = Constant which depicts the extent of surface coverage
Intraparticle diffusion	$q_t = k_3 t^{\frac{1}{2}} + A$ (14)	k <sub>3</sub> = Intraparticle diffusion rate constant (mg g <sup>-1</sup> min <sup>-1/2</sup> ) A = Constant indicating the width of the boundary layer (mg g <sup>-1</sup> ). The larger the value of A, the greater the boundary layer effect.
Particle diffusion	$-\ln\left(1 - \left(\frac{q_t}{q_e}\right)^2\right) = \frac{2\pi^2 D_p t}{r^2}$ (15)	q <sub>e</sub> = Adsorbate adsorbed per unit weight (mg g <sup>-1</sup> ) at equilibrium q <sub>t</sub> = Adsorbate adsorbed per unit weight (mg g <sup>-1</sup> ) at any time (t) C <sub>z</sub> = Ion concentration of the adsorbent (mg kg <sup>-1</sup> ). D <sub>p</sub> = Diffusion coefficient in the adsorbent phase (m <sup>2</sup> min <sup>-1</sup> ) r = Average radius of the adsorbent particles (1 × 10 <sup>-7</sup> m) t = Contact time (min)

Table 1. Cont.

Denomination	Equation	Parameters
External film diffusion	$-\ln\left(1 - \left(\frac{q_t}{q_e}\right)\right) = \frac{D_f C_s}{hr C_z} t \quad (16)$	$q_e$ = Adsorbate adsorbed per unit weight ( $\text{mg g}^{-1}$ ) at equilibrium $q_t$ = Adsorbate adsorbed per unit weight ( $\text{mg g}^{-1}$ ) at any time ( $t$ ) $D_f$ = Diffusion in the film phase surrounding the adsorbent particles ( $\text{m}^2 \text{min}^{-1}$ ) $C_s$ = Ion concentration in the solution ( $\text{mg L}^{-1}$ ) $h$ = Film thickness around the adsorbent particles ( $10^{-6}$ m in poorly stirred solutions) $r$ = Average radius of the adsorbent particles ( $1 \times 10^{-7}$ m) $t$ = Contact time (min)
Langmuir–Hinshelwood equation	$\ln \frac{C_0}{C_t} = kKt = k_{app}t \quad (17)$	$k$ = Actual rate constant ( $\text{min}^{-1}$ ) $K$ = Adsorption constant of the substrate on the nanoparticles $C_0$ = Initial concentration of the substrate ( $\text{mg L}^{-1}$ ) $C_t$ = Concentration at a specific time ( $\text{mg L}^{-1}$ ) $k_{app}$ = Apparent rate constant ( $\text{min}^{-1}$ )

## 2.1. Characterization of GO/ZTO/TO Composite

### 2.1.1. XRD and FTIR Analysis

In Figure 1a, the X-ray diffraction (XRD) patterns exhibit a pronounced peak at  $2\theta = 12.12^\circ$  ( $d = 0.73$  nm), indicative of the (0 0 1) diffraction peak characteristic of graphene oxide. Additionally, a distinct peak at  $2\theta = 26.00^\circ$  ( $d = 0.34$  nm) aligns with the (0 0 2) diffraction peak identified with graphite, as reported in the literature [55,56]. Figure 1c further presents the XRD patterns for the  $\text{ZnTiO}_3/\text{TiO}_2$  (ZTO/TO) hybrid semiconductor alongside the GO/ZTO/TO composite. The analysis shows the hybrid semiconductor consists mainly of  $\text{ZnTiO}_3$  (T), about 75% of the material, and  $\text{TiO}_2$  in its anatase phase (A), making up roughly 25% of the structure. The  $\text{ZnTiO}_3$  phase has a rhombohedral crystal structure, with lattice parameters  $a = b = 5.08$  Å and  $c = 13.93$  Å, matching the space group R-3(148) as per the COD card No. 00-026-1500. Conversely, the anatase phase of  $\text{TiO}_2$  shows a tetragonal crystal structure, with lattice dimensions  $a = b = 3.79$  Å and  $c = 9.51$  Å, adhering to the I41/amd(141) space group as detailed by COD card No. 96-901-5930.

Regarding the GO/ $\text{ZnTiO}_3/\text{TiO}_2$  (GO/ZTO/TO) composite, Figure 1b shows that this composite exhibited an XRD pattern with less intense peaks than that of the  $\text{ZnTiO}_3/\text{TiO}_2$  (ZTO/TO) hybrid oxide, particularly in the  $\text{ZnTiO}_3$  phase. Furthermore, the non-appearance of graphene reflection in the GO/ZTO/TO composite is probably due to the low amount of GO in the composite and the possible reduction in GO during the hydrothermal process [57]. The sizes of  $\text{ZnTiO}_3$  and  $\text{TiO}_2$  crystallites supported on the graphene sheets were calculated using the Scherrer formula [58] described in Equation (1) of Table 1. The calculation was carried out based on the prominent peaks of each phase, revealing an average size of 36.75 ( $\pm 2.17$ ) nm for  $\text{ZnTiO}_3$  and 24.16 ( $\pm 1.95$ ) nm for  $\text{TiO}_2$  (anatase phase).

On the other hand, Figure 2 presents the Fourier transform infrared spectroscopy (FTIR) spectra of GO, GO/ZTO/TO, and ZTO/TO.

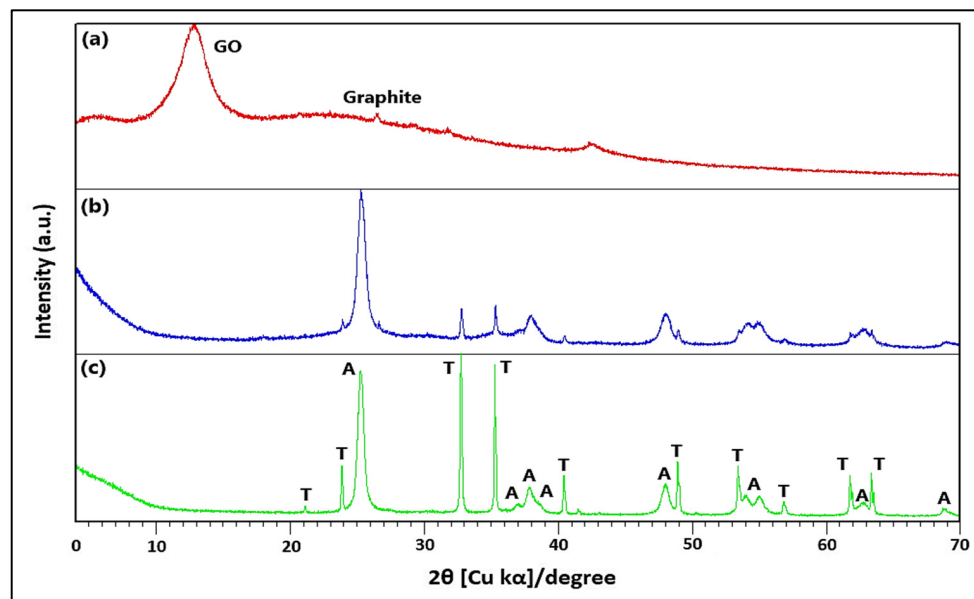


**Figure 1.** X-ray diffraction pattern of (a) GO (red line), (b) GO/ZnTiO<sub>3</sub>/TiO<sub>2</sub> (blue line), and (c) ZnTiO<sub>3</sub>/TiO<sub>2</sub> (green line). T: zinc titanate; A: anatase.

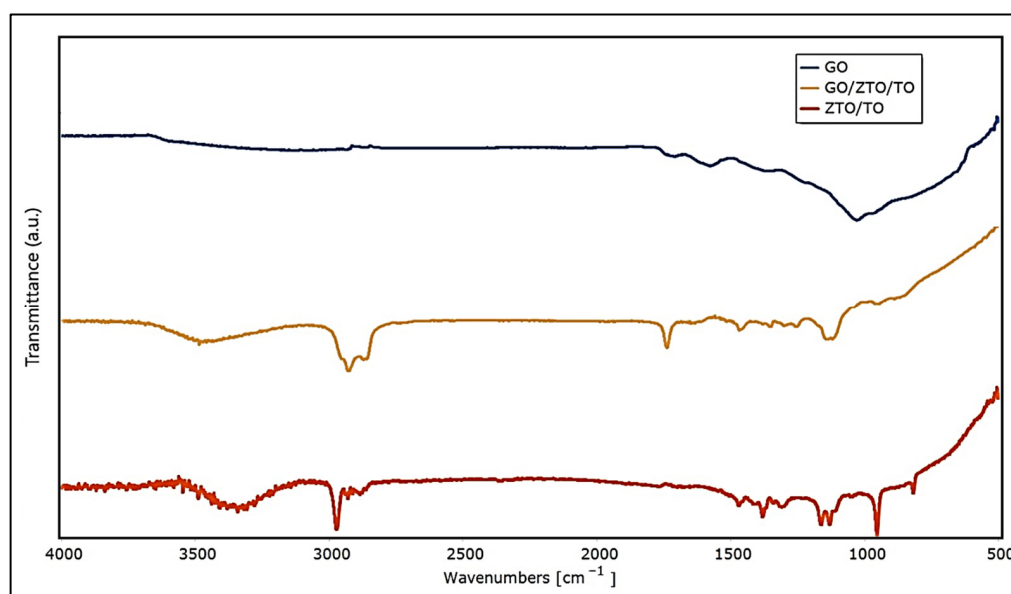


**Figure 2.** FTIR spectra of GO, GO/ZnTiO<sub>3</sub>/TiO<sub>2</sub>, and ZnTiO<sub>3</sub>/TiO<sub>2</sub>.

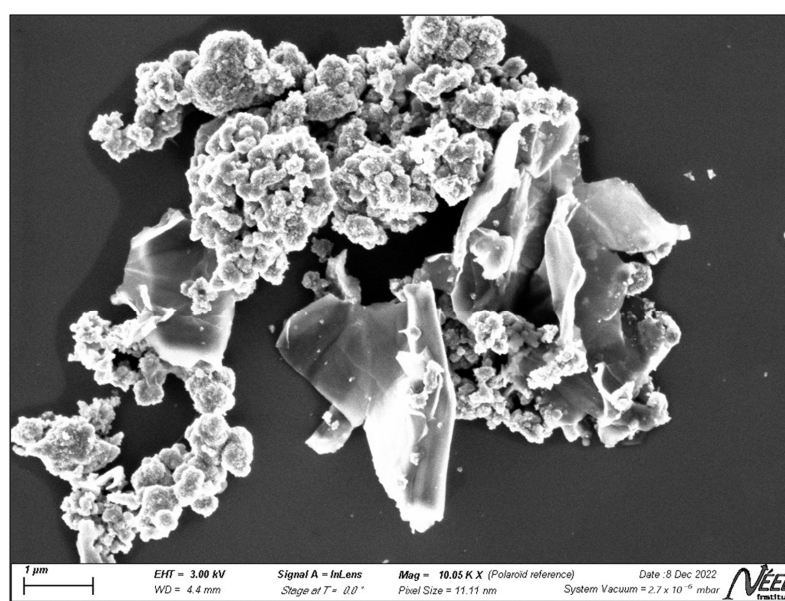
Table 2 shows the peaks and assignments for each compound, which agree with the reports of other authors [59–62].

**Table 2.** Results of FTIR analysis of GO, GO-ZTO/TO, and ZTO/TO compounds.

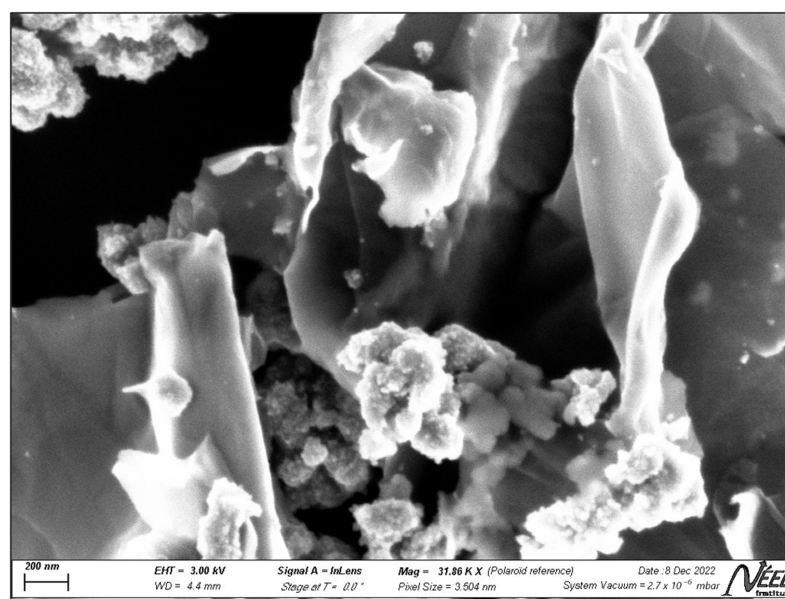
Peak	Assignment	GO (cm <sup>-1</sup> )	GO/ZTO/TO (cm <sup>-1</sup> )	ZTO/TO (cm <sup>-1</sup> )
O-H	Stretching	Not prominent	3400	3400
C-H/TiO <sub>2</sub>	Stretching	Not prominent	2920	2920
C=O	Stretching	1720	Not prominent	Not observed
C-O	Stretching/Carbonyl	~1220–1300	~1220–1300	~1220–1300
C=C	Stretching	1620	1620	Not observed
Ti-O	Metal–Oxygen bonds	Not observed	Not prominent	~500
Zn-O	Metal–Oxygen bonds	Not observed	Not prominent	~500

### 2.1.2. SEM and EDS Analysis

The SEM analysis conducted to examine the surface morphology of the synthesized material revealed that many  $\text{ZnTiO}_3/\text{TiO}_2$  nanoparticles are accumulated onto graphene nanosheets, as shown in Figure 3. This accumulation is attributed to the ease with which monomeric titanyl ions ( $\text{TiO}^{2+}$ ) adsorb onto the graphene surface due to electrostatic interactions [57], favoring the formation of the GO/ZTO/TO compound and preserving the semispherical morphology of the nanoparticles, in line with observations from previous studies [63]. Figure 3 also highlights the characteristic two-dimensional laminar structure of graphene oxide, with wrinkled surfaces and a somewhat rough texture due to the overlapping of the sheets. This roughness is related to surface defects caused by the transition from  $\text{sp}^2$  to  $\text{sp}^3$  character, resulting from a high density of oxygen-functional groups [64]. Furthermore, it is suggested that the use of ultrasound in the exfoliation of graphite oxide sheets and thermal treatment during drying can cause deformations and the folding of the laminar structures [55].



(a)



(b)

**Figure 3.** SEM photograph of GO/ZTO/TO composite at magnifications of (a) 1  $\mu\text{m}$  and (b) 200 nm.

Despite graphene oxide being found in a low proportion in the composite, a clear agglomeration of ZTO/TO nanoparticles successfully deposited on the GO surface is observed. The size measurement of these nanoparticles was carried out using the ImageJ2 v1.54 software for image analysis, determining an average size of  $27.4 \pm 5$  nm for  $\text{ZnTiO}_3/\text{TiO}_2$  nanoparticles [65,66]. These results are consistent with those obtained from the X-ray diffraction analysis (Figure 1), thereby corroborating the accuracy of the measurements.

To investigate the composition of the synthesized composite, EDS measurements were also performed. The results shown in Figure 4 display the presence of the elements C (12.93%), O (30.83%), Ti (38.65%), and Zn (17.59%) in the synthesized composite. It should be noted that the C/O ratio in graphene oxide can vary greatly from study to study due to differences in synthesis conditions [67].

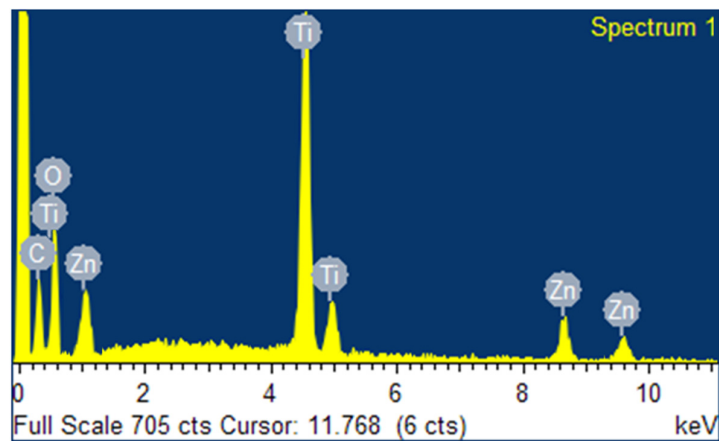


**Figure 4.** EDS spectrum of GO/ZTO/TO composite.

### 2.1.3. SSA and $\text{pH}_{\text{PZC}}$ Analysis

In this research, the specific surface area (SSA) and the volume of a monolayer for the GO/ZTO/TO composite were found to be  $111.84 \text{ m}^2/\text{g}$  and  $25.69 \text{ cm}^3/\text{g}$ , respectively. Additionally, the point of zero charge (PZC) for the composite was determined to be 6.5, as shown in Figure 5. Based on this figure, it is anticipated that the adsorbent's surface will carry a positive charge when the pH of the solution is below the PZC, and a negative charge when it exceeds the PZC. Consequently, at a pH higher than the PZC, electrostatic attractions between the negatively charged surface of the adsorbent and cationic species, such as MB dye, would be enhanced [68].

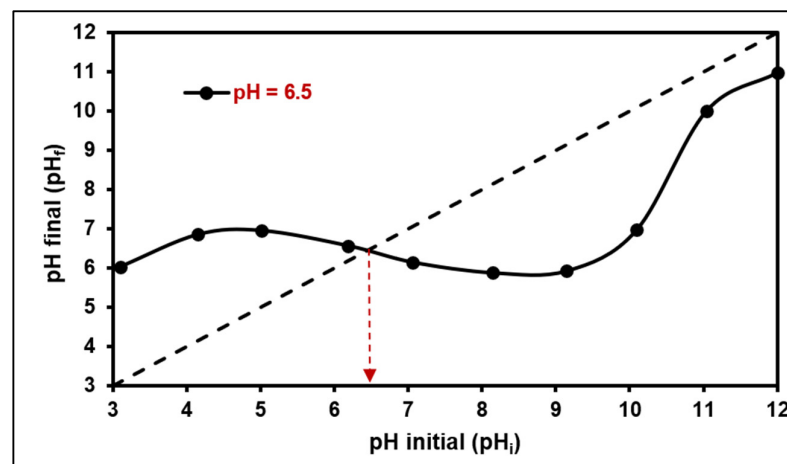


**Figure 5.** Point of zero charge ( $\text{pH}_{\text{PZC}}$ ) of GO/ZTO/TO composite. The arrow indicates the point where the curve of final pH as a function of initial pH cuts the diagonal (dashed line).

## 2.2. Adsorption Studies

Figure 6 presents the Fourier transform infrared spectroscopy (FTIR) spectra of MB, GO/ZTO/TO, and MB-GO/ZTO/TO. As can be seen in the figure, after the adsorption of MB, the FTIR spectrum of the composite shows notable changes with the appearance of new peaks at  $835\text{ cm}^{-1}$ ,  $1060\text{ cm}^{-1}$ ,  $1147\text{ cm}^{-1}$ ,  $1244\text{ cm}^{-1}$ ,  $1354\text{ cm}^{-1}$ ,  $1444\text{ cm}^{-1}$ ,  $1748\text{ cm}^{-1}$ ,  $2902\text{ cm}^{-1}$ ,  $2950\text{ cm}^{-1}$ ,  $3043\text{ cm}^{-1}$ ,  $3296\text{ cm}^{-1}$ ,  $3310\text{ cm}^{-1}$ ,  $3362\text{ cm}^{-1}$ ,  $3410\text{ cm}^{-1}$ ,  $3460\text{ cm}^{-1}$ ,  $3498\text{ cm}^{-1}$ ,  $3542\text{ cm}^{-1}$ ,  $3567\text{ cm}^{-1}$ , and  $3750\text{ cm}^{-1}$ . These peaks reflect the complex interaction between the GO/ZTO/TO composite and MB, evidencing both physical and chemical interactions.

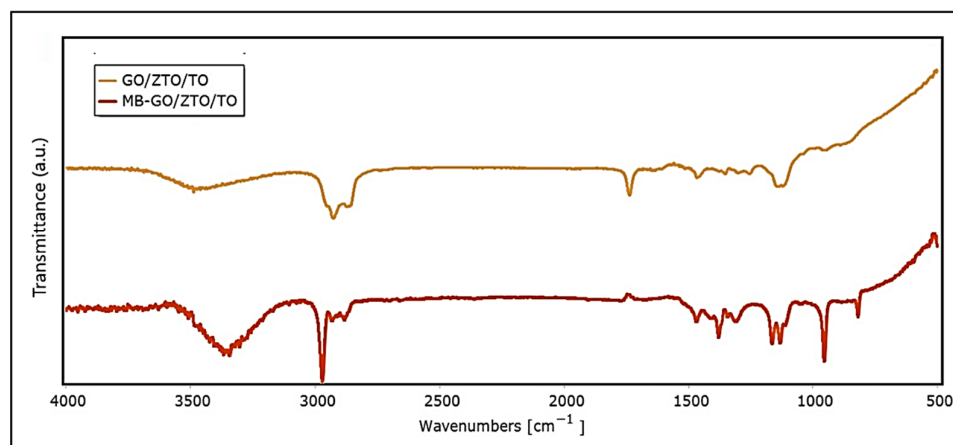


**Figure 6.** FTIR spectra of MB, GO/ZnTiO<sub>3</sub>/TiO<sub>2</sub>, and MB-GO/ZnTiO<sub>3</sub>/TiO<sub>2</sub>.

Table 3 shows the peaks and assignments for each compound, which agree with the reports of other authors [69–71].

**Table 3.** Results of FTIR analysis of MB, GO/ZTO/TO, and MB-GO/ZTO/TO.

Peak	Assignment	GO/ZTO/TO (cm <sup>-1</sup> )	MB-GO/ZTO/TO (cm <sup>-1</sup> )
Ti-O	Metal–Oxygen bonds	Not prominent	~500
Zn-O	Metal–Oxygen bonds	Not prominent	~500
C-H	Bending vibrations	Not observed	835
S=O	Stretching vibrations	Not observed	1060–1244
C-O	Stretching/Carbonyl	1220–1300	1220–1300
C-N/N-H	Stretching and bending vibrations	Not observed	1354–1444
C=C	Stretching	1620	Not prominent
C=O	Stretching vibrations	1720	1748
C-H/O-H	Stretching vibrations	3400–3600	3400–3600

### 2.2.1. Effect of pH on MB Adsorption

Figure 7 illustrates the efficiency of the GO/ZTO/TO composite in removing MB dye, indicating successful adsorption at acidic pH levels beneath its point of zero charge ( $\text{pH}_{\text{PZC}} = 7.0$ ). Additionally, the figure demonstrates that raising the pH of the dye solution amplifies the adsorption of cationic MB dye molecules onto the GO/ZTO/TO surface [72,73].

Given that electrostatic attraction enhances the adsorption of cationic dyes when  $\text{pH} > \text{PZC}$  [74], a  $\text{pH}$  of  $7.0 \pm 0.1$  was chosen for the dye solution in further adsorption experiments. Notably, the literature indicates that GO remains stable within a  $\text{pH}$  range of 4 to 10 [75].

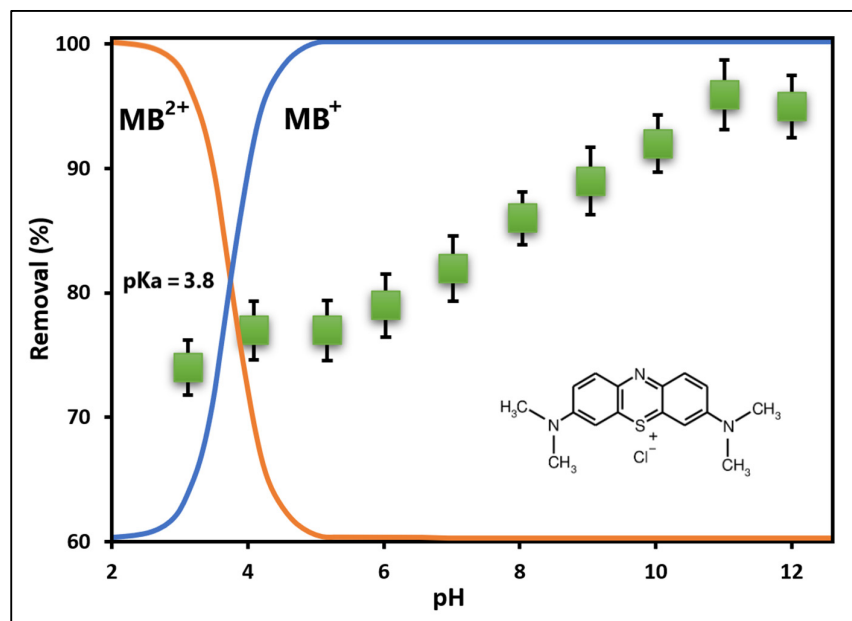


Figure 7. Effect of pH on the MB adsorption.

### 2.2.2. Effect of MB Dosage

The influence of the initial dye concentration on adsorption correlates with the dye concentration and available sites on the adsorbent. The impact of the initial concentration of MB on the adsorption efficiency of GO/ZTO/TO was evaluated by analyzing the residual MB in the solution through UV–Vis spectrophotometry at  $\lambda = 623$  nm, utilizing Equation (2) from Table 1. The maximum adsorption of GO/ZTO/TO was determined from equilibrium isotherms at different initial concentrations of MB, ranging from 1.5 to 50 mg L<sup>-1</sup>. Figure 8 illustrates the fitting of experimental data to the Langmuir, Freundlich, and Temkin isotherm models, represented by Equations (3)–(5) in Table 1, respectively. According to Figure 8, the Langmuir isotherm model provided the best fit.

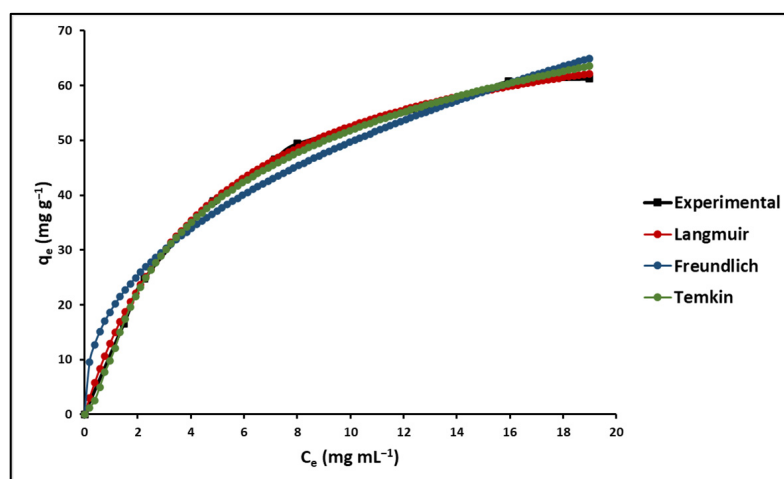


Figure 8. Effect of concentration on the MB adsorption.

Isotherm parameters are detailed in Table 4. The Langmuir isotherm showed a separation factor ( $R_L$ ) of 0.23, signifying favorable adsorption ( $0 < R_L < 1$ ) for the composite [76]. Constants for the Langmuir, Freundlich, and Temkin models, calculated at temperatures of 293.15 K, 303.15 K, and 313.15 K, are listed in Table 4. Here, the  $R_L$  values range from 0 to 1, and the “ $n$ ” coefficient, indicating adsorption intensity, spans from 1 to 10. Hence, it can be deduced that MB dye adsorption onto GO/ZTO/TO is effectively favorable.

**Table 4.** Isotherm parameters for MB adsorption on GO/ZTO/TO at different temperatures.

Isotherm Parameters		293.15 K	303.15 K	313.15 K
Langmuir	$q_{\max}$ (mg g <sup>-1</sup> )	77.95 (±2.15)	86.69 (±1.95)	95.97 (±2.56)
	$K_L$ (L mg <sup>-1</sup> )	0.04 (±0.03)	0.08 (±0.02)	0.22 (±0.04)
	$R_L$	0.56	0.38	0.19
	$\chi^2$	2.57	2.36	2.97
	$R^2$	0.98	0.97	0.99
Freundlich	$K_F$ (L mg <sup>-1</sup> )	18.98 (±2.18)	21.11 (±2.87)	23.37 (±2.34)
	$N$	2.39 (±0.36)	2.66 (±0.40)	2.94 (±0.61)
	$1/n$	0.42	0.38	0.34
	$\chi^2$	2.84	3.14	2.95
	$R^2$	0.94	0.93	0.95
Temkin	$B$	18.35 (±1.26)	20.41 (±1.78)	22.59 (±1.97)
	$A$	1.68 (±0.29)	1.87 (±0.37)	2.07 (±0.35)
	$\chi^2$	2.62	3.08	2.91
	$R^2$	0.96	0.95	0.97

### 2.2.3. Effect of Temperature on MB Adsorption

The adsorption process is significantly influenced by the temperature of the solution, with thermodynamic parameters shedding light on the feasibility and spontaneity of a process [77]. To evaluate these parameters, namely the Gibbs free energy change ( $\Delta G^\circ$ ), enthalpy change ( $\Delta H^\circ$ ), and entropy change at the surface ( $\Delta S^\circ$ ), the equilibrium constant was calculated at different temperatures using Equations (6)–(9) listed in Table 1. The outcomes of this analysis are illustrated in Figure 9.

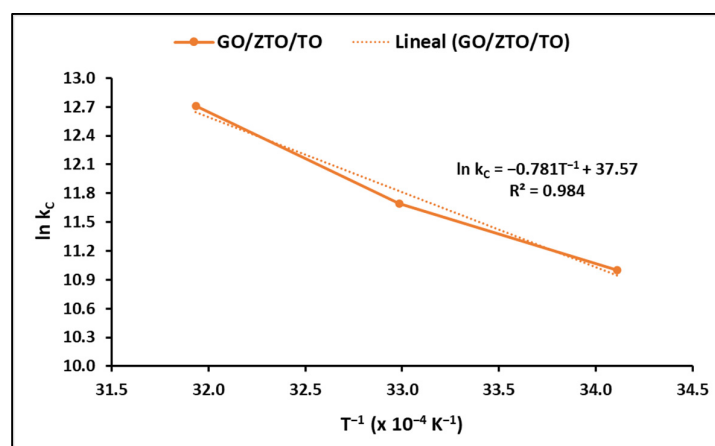
**Figure 9.** Thermodynamic analysis of MB adsorption on GO/ZTO/TO.

Table 5 outlines the determined thermodynamic parameters. The  $\Delta G^\circ$  values reflect the spontaneity of the adsorption process, with more negative values indicating a higher favorability. Conversely, a positive  $\Delta H^\circ$  value denotes the endothermic nature of the process, and a positive  $\Delta S^\circ$  value indicates increased randomness at the interface between the solution and the solid during adsorption.

**Table 5.** Thermodynamic parameters of the MB adsorption on GO/ZTO/TO.

Temperature (K)	$\ln k_C$	$\Delta G^\circ$ (kJ mol <sup>-1</sup> )	$\Delta H^\circ$ (kJ mol <sup>-1</sup> )	$\Delta S^\circ$ (kJ mol <sup>-1</sup> K <sup>-1</sup> )
293.15	11.00	−26.81		
303.15	11.70	−29.28	64.90	0.31
313.15	12.71	−33.08		

### 2.2.4. Effect of Contact Time on MB Adsorption

The dynamics of MB adsorption onto GO/ZTO/TO were explored in this research, utilizing three kinetic models: pseudo-first-order (Lagergren), pseudo-second-order (Ho), and the Elovich model. The fitting of experimental data to these models is illustrated in Figure 10, based on Equations (11)–(13) listed in Table 1.

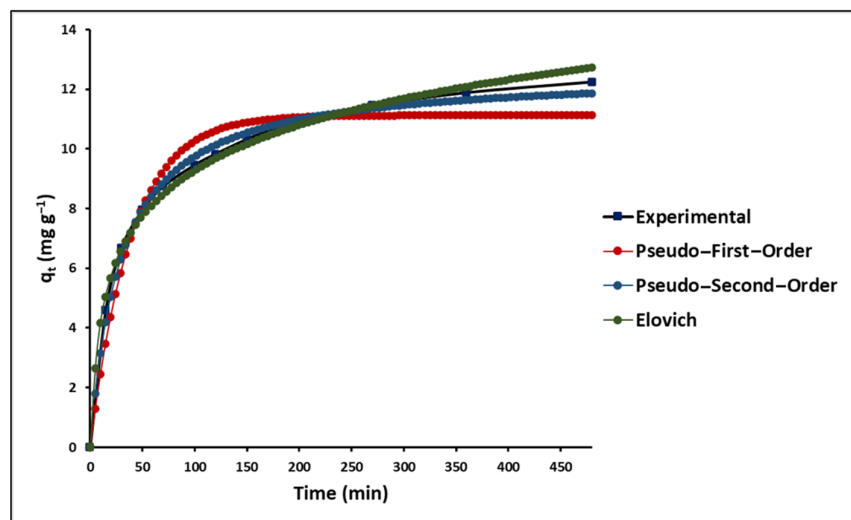


Figure 10. Adsorption kinetics of MB onto GO/ZTO/TO.

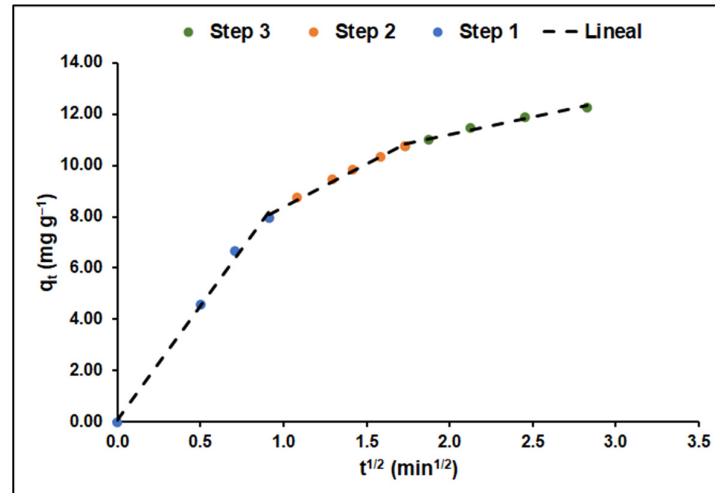
Figure 10 depicts the adsorption kinetics of MB on GO/ZTO/TO, showing a swift initial adsorption phase followed by a slower adsorption stage. According to Table 6, the pseudo-second-order model most accurately captures the adsorption kinetics of MB on GO/ZTO/TO, aligning with findings from previous studies [78].

Table 6. Kinetic parameters for MB adsorption onto GO/ZTO/TO.

Kinetic Parameters		293.15 K
Pseudo-first-order	$q_{max}$ (mg g <sup>-1</sup> )	11.13 (±0.29)
	$k_1$ (L mg <sup>-1</sup> )	0.03 (±2.92 × 10 <sup>-3</sup> )
	$\chi^2$	0.50
	$R^2$	0.96
Pseudo-second-order	$q_{max}$ (mg g <sup>-1</sup> )	12.58 (±0.16)
	$k_2$ (L mg <sup>-1</sup> )	2.74 × 10 <sup>-3</sup> (±1.89 × 10 <sup>-4</sup> )
	$\chi^2$	0.06
	$R^2$	1.00
Elovich	$\alpha$	30.82 (±5.61)
	$\beta$	0.02 (±9.39 × 10 <sup>-4</sup> )
	$\chi^2$	6.34
	$R^2$	0.98
Intraparticle diffusion	$k$ (mg g <sup>-1</sup> min <sup>-1/2</sup> )	0.51 (±0.06)
	$A$	3.24 (±0.85)
	$R^2$	0.82
External film diffusion	$D_f$ (m <sup>2</sup> min <sup>-1</sup> )	9.90 × 10 <sup>-12</sup>
	$R^2$	0.83
Internal pore diffusion	$D_p$ (m <sup>2</sup> min <sup>-1</sup> )	7.24 × 10 <sup>-18</sup>
	$R^2$	0.91

Figure 11, illustrating the adaptation to the intraparticle diffusion model and based on Equation (14) from Table 1, delineates the MB adsorption on GO/ZTO/TO in three

distinct phases: a rapid initial phase ( $k_1 = 8.88 \text{ mg g}^{-1} \text{ min}^{-1/2}$ ), a slower secondary phase ( $k_2 = 3.34 \text{ mg g}^{-1} \text{ min}^{-1/2}$ ), and a final equilibrium phase ( $k_3 = 1.37 \text{ mg g}^{-1} \text{ min}^{-1/2}$ ). The kinetic constants for each phase, alongside the effective diffusion coefficients  $D_f$  and  $D_p$ , derived from Equations (15) and (16) in Table 1, are detailed in Table 6.



**Figure 11.** Adsorption kinetics of MB on GO/ZTO/TO.

As detailed in Figure 11, the initial phase is marked by swift diffusion of MB molecules towards the GO/ZTO/TO surface, transitioning to a reduced diffusion rate in the second phase, likely due to the ongoing adsorption process. The final phase, exhibiting the slowest rate, indicates approaching equilibrium, influenced by the diminished MB concentration in the solution and fewer available active sites on the adsorbent.

### 2.3. Photodegradation Studies

Figure 12 displays the outcomes of the photodegradation experiments, clearly showing that the composite achieved the highest level of MB photodegradation after 60 min of exposure to UVC light.

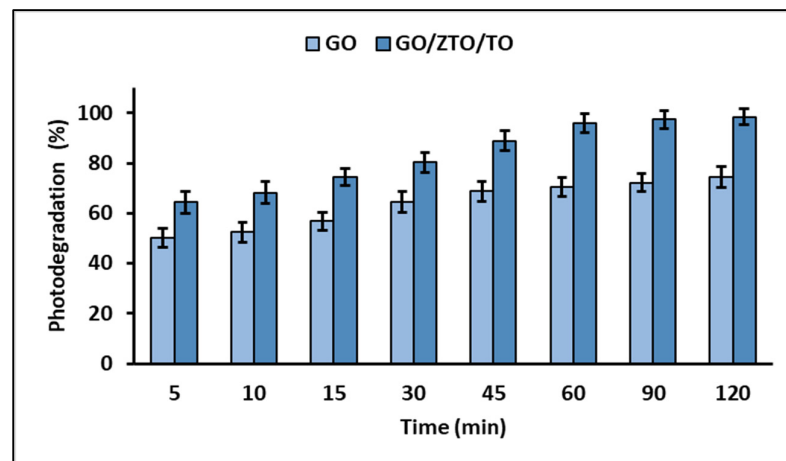


**Figure 12.** MB photodegradation capacity of GO and GO/ZTO/TO.

The Langmuir–Hinshelwood equation demonstrated a linear correlation between  $\ln(C_0/C_t)$  and time, indicating that the photocatalytic degradation of MB adheres to pseudo-first-order kinetics. The calculated apparent rate constants ( $k_{app}$ ) for MB photodegradation with GO and the GO/ZTO/TO composite were found to be  $0.0241 \text{ min}^{-1}$  and  $0.0653 \text{ min}^{-1}$ , respectively.

#### 2.4. Reusability of GO/ZTO/TO for MB Removal

Figure 13 shows the efficiency of MB removal by the GO/ZTO/TO composite for five consecutive cycles, each lasting 60 min. After each removal cycle, the composite was washed with methanol, dried, and evaluated again under the same conditions as the previous cycle. After the fifth cycle, the MB adsorption capacity of GO/ZTO/TO decreased by only 15%.

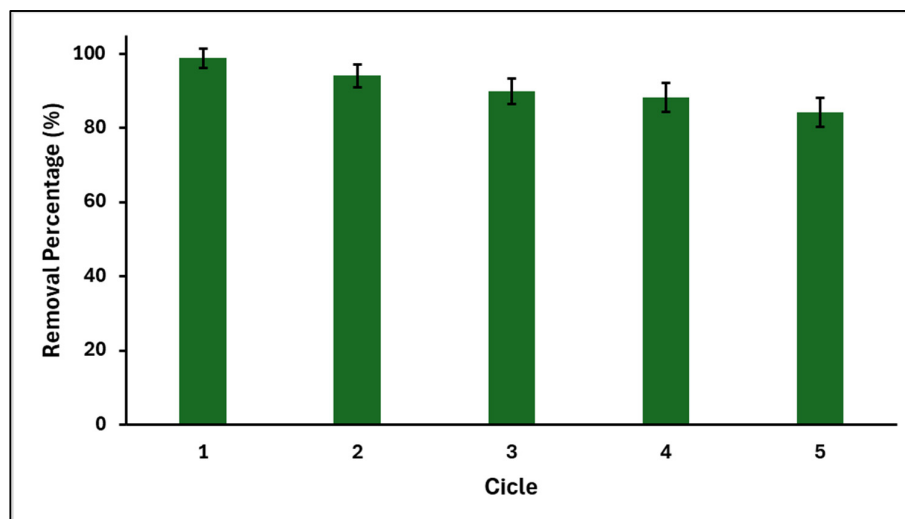


**Figure 13.** MB removal efficiency of the GO/ZTO/TO composite for five cycles (MB concentration = 20 mg L<sup>-1</sup>, solution pH = 7.0 ± 0.1, temperature = 20 °C, n = 3).

### 3. Discussion

#### 3.1. Characterization of GO/ZTO/TO

The characterization of the GO/ZnTiO<sub>3</sub>/TiO<sub>2</sub> composite using various techniques has revealed detailed information on its physicochemical, structural, and morphological properties. X-ray diffraction (XRD) demonstrated the presence of well-defined crystalline phases corresponding to graphene oxide (GO), ZnTiO<sub>3</sub>, and TiO<sub>2</sub>, with crystallite sizes that favor surface reactivity due to their nanometric scale. This aspect is important for photocatalysis since more reactive surfaces can generate a greater amount of reactive oxygen species, which are essential for the photodegradation of contaminants.

In FTIR spectroscopy analysis, the comparison of graphene oxide (GO) with GO/ZnTiO<sub>3</sub>/TiO<sub>2</sub> (GO/ZTO/TO) and ZnTiO<sub>3</sub>/TiO<sub>2</sub> (ZTO/TO) reveals significant interactions that influence the characteristics of the material. GO only exhibits distinct bands related to oxygen-containing functional groups, such as carboxyl groups around 1720 cm<sup>-1</sup>, which become less pronounced in the GO/ZTO/TO composite, suggesting a possible interaction between the carboxyl groups of GO and the ZTO/TO matrix. These changes could affect the surface availability of these groups, impacting the properties of the material and its performance in adsorption processes. The ZTO/TO spectrum shows small specific peaks around 500 cm<sup>-1</sup>, attributed to metal oxide bonds such as Zn-O and Ti-O, which are indicative of the successful integration of ZnTiO<sub>3</sub> and TiO<sub>2</sub> within the composite. The reduced presence of these peaks in the GO or GO/ZTO/TO spectra suggests that GO incorporation may influence the accessibility or state of these metal oxide bonds, possibly pointing to an electrostatic interaction between graphene oxide and the ZnTiO<sub>3</sub>/TiO<sub>2</sub> components. Electrostatic interactions within compounds such as GO/ZTO/TO can be complex, as the various functional groups and active sites can carry charges. For example, the oxygenated groups of GO, when ionized in aqueous solutions, confer a net surface charge that can attract oppositely charged species. This is particularly relevant in adsorption systems where charged contaminants, such as cationic dyes such as methylene blue, are attracted to negatively charged sites on the GO surface. The addition of ZnTiO<sub>3</sub>/TiO<sub>2</sub>

could alter the density and distribution of these fillers, thereby improving the interaction of the composite with the dye. The introduction of  $\text{ZnTiO}_3$  and  $\text{TiO}_2$  into the GO matrix is not only a structural combination but also causes functional changes. These changes facilitate the adsorption of contaminants through charge interactions, confirming the suitability of the compound to treat contaminated water.

Scanning electron microscopy (SEM) revealed a unique morphology of the composite, with  $\text{ZnTiO}_3/\text{TiO}_2$  nanoparticles distributed on the GO sheets, which not only prevents excessive nanoparticle agglomeration and facilitates light scattering, but also improves the accessibility of contaminants to active sites for adsorption and subsequent photodegradation. This porous structure, evidenced in the SEM images, together with a considerably high specific surface area, determined by specific surface area (SSA) analysis, provides an optimal environment for contaminant capture.

Regarding X-ray energy dispersive spectroscopy (EDS), this technique confirmed the elemental composition of the compound, highlighting the successful integration of the components that make up GO/ZTO/TO. This composition is key to the stability of the material and its efficiency in removing contaminants. Indeed, in this study, the synergy between the components was evident, which allowed for improvement in both the adsorption and the photocatalytic activity of the composite material.

Measurement of the point of zero charge ( $\text{pH}_{\text{PZC}}$ ) of the compound at 6.5 suggests that the surface will become negatively charged in solutions with a pH higher than this value, favoring the adsorption of positively charged contaminants such as methylene blue through electrostatic interactions. This property is especially relevant for the optimization of treatment conditions, allowing the adaptation of the process to the specific characteristics of the wastewater to be treated.

Taken together, the physicochemical, structural, and morphological properties of the GO/ZTO/TO composite illustrate its ability to be an effective adsorbent and photocatalyst. The interaction between the components of the compound not only improves the stability and adsorption capacity but also enhances the photocatalytic activity under irradiation, highlighting its potential for water purification through the efficient removal of complex organic contaminants such as methylene blue.

### 3.2. Adsorption Studies

In the study of GO/ZTO/TO composites, both in the presence and absence of methylene blue (MB), significant changes observed through FTIR spectroscopy provide deep insights into the chemical interactions and structural modifications within these materials. The peak at  $835\text{ cm}^{-1}$  could indicate C-H out-of-plane bending vibrations in substituted benzene rings, possibly reflecting  $\pi$ - $\pi$  interactions between the composite and MB aromatic rings. This suggests an interaction between GO and MB where the aromatic structures of GO may play a significant role in MB adsorption. Peaks in the range of  $1060\text{ cm}^{-1}$  to  $1244\text{ cm}^{-1}$  indicative of S=O vibrations suggest the interaction of sulfonate groups of MB with the composite surface. This implies a possible electrostatic interaction or coordination with active sites on the composite, facilitated by the presence of  $\text{ZnTiO}_3$  and  $\text{TiO}_2$ , which can offer sites for the adsorption of sulfonate groups. Peaks in the range of  $1354\text{ cm}^{-1}$  to  $1444\text{ cm}^{-1}$ , corresponding to C-N stretching and N-H bending vibrations, signal the interaction between the composite and the amine functional groups of MB. This could involve the formation of hydrogen bonds between the amine groups of MB and the oxygen-containing groups of GO. The peak at  $1748\text{ cm}^{-1}$ , suggesting C=O stretching vibrations, could be associated with the chemical or physical modification of carboxylic groups in GO upon MB adsorption, or it might indicate interactions with  $\text{TiO}_2$  or  $\text{ZnTiO}_3$ . The presence of multiple peaks between  $3400\text{ cm}^{-1}$  and  $3600\text{ cm}^{-1}$  after MB adsorption underscores the complexity of the interactions at play. These peaks suggest a wide range of C-H vibrations and the formation of numerous hydrogen bonds, possibly between MB and the hydroxyl or carboxyl groups on GO, as well as interactions with the surfaces of  $\text{TiO}_2$  and  $\text{ZnTiO}_3$ . This region is particularly telling of the specific interactions contributing to the composite's

ability to adsorb MB, suggesting that both physical interactions (such as  $\pi$ - $\pi$  stacking and electrostatic attractions) and chemical interactions (like hydrogen bonding and van der Waals forces) are crucial for the adsorption process.

### 3.2.1. Effect of pH on MB Adsorption

The influence of pH on the adsorption of methylene blue (MB) on graphene oxide/ZnTiO<sub>3</sub>/TiO<sub>2</sub> (GO/ZTO/TO) composite provides valuable insight into the interaction between adsorbent and adsorbate. This relationship highlights the importance of surface charges on the adsorbent and dye speciation in solution, which vary significantly with pH [79]. The existence of MB (pK<sub>a</sub> = 3.8) in aqueous solutions as an undissociated molecule (MB<sup>0</sup>) and as a cationic species (MB<sup>+</sup>) establishes a basis for understanding how pH affects its interaction with the compound [80].

It has been observed that the adsorption capacity of MB by GO/ZTO/TO increases with increasing solution pH, reaching an optimum near pH = 7.0. However, this capacity decreases at pH 12, attributed to the destabilization of GO and the creation of positively charged sites on its surface, leading to an electrostatic repulsion with MB molecules [81,82]. In acidic environments, the protonation of oxygen-functional groups on the surface of GO/ZTO/TO generates a positive surface charge, repelling the cationic MB. As the pH increases, these groups are deprotonated, resulting in a more negatively charged surface that favors the adsorption of MB through electrostatic attraction [75].

The high adsorption capacity observed at alkaline pH values is attributed to the increase in hydroxyl ions, resulting in a greater electrostatic attraction between the MB<sup>+</sup> cationic species and the negatively charged surface of the composite [83]. However, at highly alkaline pH levels, OH ions can form complexes with other ions, such as MB<sup>+</sup>, potentially influencing the adsorption of the dye on the adsorbent surface [84]. This phenomenon could result in the precipitation of dye molecules on the surface of the composite. Therefore, the adsorption mechanism at alkaline pH is probably a combination of electrostatic attraction and precipitation [85]. On the other hand, it is shown that graphene oxide has a reasonably good MB<sup>+</sup> adsorption capacity at pH < pH<sub>PZC</sub>, where electrostatic interactions do not favor adsorption. Under these experimental conditions (pH < 6.5), it is suggested that the adsorption of the dye could occur via ion exchange since the cationic species MB<sup>+</sup> would be competing with H<sup>+</sup> for the active sites on the surface of GO/ZTO/TO [86].

### 3.2.2. Effect of Initial Concentration of MB

The adsorption capacity of the GO/ZTO/TO composite toward methylene blue (MB) provides deep insights into the molecular interactions and effectiveness of the material in purification applications. The evaluation of adsorption using the Langmuir, Freundlich, and Temkin isothermal models revealed a favorable correspondence with the Langmuir model, suggesting monolayer adsorption on the homogeneous surfaces of the compound. This behavior indicates a specific and uniform interaction between the MB and the active sites of the compound, a crucial aspect for purification applications where high selectivity and efficiency are required. From the Langmuir model, the maximum adsorption capacity was estimated ( $q_{\text{max}} = 77.95 \text{ mg g}^{-1}$ ), which reflects the maximum amount of MB that can be adsorbed per unit mass of the compound under optimal conditions. Furthermore, the Langmuir separation factor ( $R_L$ ) was found to be in the range of  $0 < R_L < 1$  for the initial MB concentrations tested, indicating that adsorption is favorable under the experimental conditions used. It is worth mentioning that  $R_L$  values between 0 and 1 suggest favorable adsorption, while  $R_L > 1$  would indicate unfavorable adsorption. The fit of the data to the Langmuir model, as well as the  $R_L$  values, not only indicate the feasibility and favorability of MB adsorption on the composite but also that the surface saturation occurs in a monolayer. This is indicative of a high affinity between the MB and the composite, possibly due to  $\pi$ - $\pi$  interactions between the aromatic rings of the MB and the graphene

structure of the composite, as well as possible electrostatic interactions depending on the pH of the solutions.

The coefficients obtained from the Freundlich model, especially the value of  $n$ , which is between 1 and 10, suggest that the adsorption is physical and favorable. The physical nature of adsorption is beneficial from the perspective of adsorbent reuse, as physical interactions are generally easier to reverse than chemical ones, facilitating compound regeneration.

The preference of the Langmuir model in the description of the adsorption of MB over GO/ZTO/TO highlights the formation of a uniform adsorption layer and the existence of a defined maximum adsorption capacity, essential for the design of predictive and efficient treatment processes. An interpretation of the results suggests that pH adjustments can significantly influence the adsorption capacity of the compound, optimizing the interaction between MB and the compound by manipulating the surface charge and the availability of active sites.

### 3.2.3. Effect of Temperature on MB Adsorption

The effect of temperature on the adsorption of methylene blue (MB) onto the GO/ZTO/TO composite is important for understanding the thermodynamic nature of the adsorption process. The increase in the adsorption capacity of MB on the GO/ZTO/TO composite with increasing temperature indicates an endothermic process. This behavior suggests a higher affinity between the MB and the composite at higher temperatures, probably due to the higher mobility of the MB molecules and the expansion of the pores in the composite, which facilitates access to more adsorption sites.

The thermodynamic parameters obtained, such as the change in Gibbs free energy ( $\Delta G^\circ$ ), enthalpy ( $\Delta H^\circ$ ), and entropy ( $\Delta S^\circ$ ), confirm the endothermic nature of the process. Negative values of  $\Delta G^\circ$  at different temperatures indicate that the adsorption is spontaneous, while a positive value of  $\Delta H^\circ$  reinforces the idea that the process is endothermic. The positive increase in  $\Delta S^\circ$  suggests an increase in disorder at the solid–liquid interface during adsorption. The relationship between temperature increases and improvement in adsorption capacity could be exploited to optimize MB removal efficiency in practical applications, allowing adjustments in operating parameters to maximize process efficiency.

### 3.2.4. Effect of Contact Time on MB Adsorption

The adsorption kinetics of methylene blue (MB) on the GO/ZTO/TO composite demonstrate adherence to the pseudo-second-order model, indicating that the adsorption rate depends on both the amount of MB adsorbed at equilibrium and the amount of MB adsorbed at any given time. This fit to the pseudo-second-order model suggests that the rate-limiting step is the chemical interaction between the MB and the active sites on the composite surface. The high values of the correlation coefficient ( $R^2$ ) for this model indicate a good fit to the experimental data, reflecting the applicability of the model to describe the adsorption kinetics of the GO/ZTO/TO-MB system.

The fit with the pseudo-second-order model highlights the characteristics of GO/ZTO/TO as a material with active sites capable of chemically interacting with MB molecules, facilitating efficient adsorption. This observation is consistent with the implications of the Langmuir isotherm observed in this study, where the formation of a monolayer of MB on the composite surface indicates that adsorption occurs at specific sites with uniform adsorption energy.

On the other hand, the adsorption of MB on GO/ZTO/TO shows a typical intraparticle diffusion behavior, where three different stages were identified based on the kinetic constant of each stage. The first stage, characterized by a high kinetic constant, corresponds to the external diffusion of MB towards the GO/ZTO/TO surface. The second stage, with a lower kinetic constant, reflects the intraparticle diffusion of MB within the composite pores. Finally, the last stage, with the lowest kinetic constant, indicates the adsorption equilibrium where the adsorption rate decreases due to the saturation of the adsorption sites.

The diffusion coefficients in the outer film phase ( $D_f$ ) and in the adsorbent phase ( $D_p$ ) provide information on the resistance to mass transfer during the adsorption process. In this study, the values of ( $D_f$ ) and ( $D_p$ ) indicate that both intraparticle diffusion and mass transfer across the outer film boundary contribute significantly to the adsorption kinetics, which is consistent with the results obtained through kinetic models.

The maximum adsorption capacity ( $q_{max}$ ) of methylene blue (MB) on the GO/ZTO/TO composite synthesized in this study, which is reported as  $77.95 \text{ mg g}^{-1}$ , provides an interesting comparison with a variety of adsorbents previously reported in the literature. As seen in Table 7, the MB adsorption capacity of the composite is comparable to that of other adsorbents based on graphene and its compounds.

**Table 7.** Calculated values of absorption energy.

Adsorbent	Adsorption Capacity ( $\text{mg g}^{-1}$ )	Reference
Reduced GO	68	[87]
Multi-wall Carbon Nanotube	48	[88]
PMMA-rGO	699	[89]
$\kappa$ -Carrageenan/GO gel beads	658	[90]
$\text{Fe}_3\text{O}_4/\text{GO@MF}$	418	[91]
PT-GO	257	[92]
GO/calcium alginate	182	[93]
Graphene-carbon nanotube	82	[94]
Graphene nanosheet/ $\text{Fe}_3\text{O}_4$	44	[95]
GO/ $\text{Co}_3\text{O}_4$	40	[96]
MgO/GO	172	[97]
CS/ $\text{Fe}_3\text{O}_4/\text{GO}$	30	[98]
CMC-Alg/GO	45	[99]
GO@ $\text{ZrO}_2$	23	[100]
GO-CNT/AC	175	[101]
GO/ $\text{ZnTiO}_3/\text{TiO}_2$	78	This study

The adsorption capacities of various adsorbents shown in Table 7 exhibit a wide range, suggesting that the adsorption efficiency may largely depend on the specific material composition and structure of the adsorbents, as well as the nature of the adsorbate. From the table, it can be evident that polymethylmethacrylate-reduced graphene oxide (PMMA-rGO) and  $\kappa$ -carrageenan/GO gel beads show exceptionally high adsorption capacities at  $699 \text{ mg g}^{-1}$  and  $658 \text{ mg g}^{-1}$ , respectively. These values are significantly higher compared to the adsorption capacity obtained in this study for GO/ $\text{ZnTiO}_3/\text{TiO}_2$  ( $78 \text{ mg g}^{-1}$ ), indicating that the inclusion of certain polymers or biomaterials with GO can improve the adsorption performance, possibly due to the introduction of additional functional groups or increased porosity. The  $\text{Fe}_3\text{O}_4/\text{GO@MF}$  adsorbent also exhibits a high adsorption capacity of  $418 \text{ mg g}^{-1}$ , which is more than five times higher than that of GO/ $\text{ZnTiO}_3/\text{TiO}_2$ . This could be attributed to the magnetic properties of  $\text{Fe}_3\text{O}_4$ , which could facilitate the separation process and improve the adsorption efficiency. Interestingly, PT-GO and GO/calcium alginate, with capacities of  $257 \text{ mg g}^{-1}$  and  $182 \text{ mg g}^{-1}$ , show that modifying GO with various treatments or combining it with other materials can lead to better performance. Likewise, the reduced GO itself has a reported capacity of  $68 \text{ mg g}^{-1}$ , which is slightly lower than the capacity observed in this study for GO/ $\text{ZnTiO}_3/\text{TiO}_2$ . This could be indicative of the synergistic effects introduced by the combination of  $\text{ZnTiO}_3/\text{TiO}_2$  with GO. At the lower end of the spectrum, GO@ $\text{ZrO}_2$ , CMC-Alg/GO, and CS/ $\text{Fe}_3\text{O}_4/\text{GO}$  have capacities of  $23 \text{ mg g}^{-1}$ ,  $45 \text{ mg g}^{-1}$ , and  $30 \text{ mg g}^{-1}$ , respectively. These capacities are below the capacity reported for GO/ $\text{ZnTiO}_3/\text{TiO}_2$  in this study, suggesting that not all compounds or modifications result in improved adsorption capacities. It is essential to consider that the variation in adsorption capacities can also be influenced by the experimental conditions, the nature of the MB solution, and the presence of competing ions or molecules. The adsorbent capacity of the GO/ $\text{ZnTiO}_3/\text{TiO}_2$  composite is relatively

modest compared to other materials. However, its photocatalytic potential contributes to improving the efficiency of the composite for the removal of dye from aqueous solutions. In addition, the GO/ZTO/TO composite offers other advantages, such as ease of separation, cost-effectiveness, and recyclability, which are also crucial factors for real-world applications. Therefore, while adsorption capacity is an important metric, it is not the only factor that determines the suitability of an adsorbent for practical use. Other considerations such as material stability, reusability, operational cost, and environmental impact are equally important for a whole evaluation of adsorbent performance.

### 3.3. Photodegradation Studies

The photodegradation of contaminants, such as methylene blue (MB), in the presence of the GO/ZTO/TO compound represents an advanced approach to water purification that addresses key limitations associated with conventional adsorption methods. While adsorption transfers the contaminant from one matrix to another, requiring the subsequent handling of the contaminated adsorbent, photocatalysis offers a route for the degradation of the adsorbed contaminant into less toxic molecules, potentially simplifying waste management.

The current study demonstrates that the photocatalytic degradation of MB follows pseudo-first-order kinetics, as indicated by the Langmuir–Hinshelwood equation, evidencing a linear correlation between  $\ln(C_0/C_t)$  and time. The values of the apparent rate constants ( $k_{app}$ ) for the photodegradation of MB with GO and the GO/ZTO/TO composite were  $0.0241 \text{ min}^{-1}$  and  $0.0653 \text{ min}^{-1}$ , respectively. These results highlight the higher photocatalytic efficiency of the GO/ZTO/TO composite compared to GO alone, suggesting that the inclusion of  $\text{ZnTiO}_3$  and  $\text{TiO}_2$  in the GO matrix significantly improves the photocatalytic activity.

The difference in apparent rate constants between GO alone and the GO/ZTO/TO composite underlines the impact of the synergy between the composite components on the photodegradation efficiency. The presence of  $\text{ZnTiO}_3$  and  $\text{TiO}_2$ , known for their photocatalytic properties under UV irradiation, could provide additional active sites and pathways for the generation of reactive oxygen species, facilitating the degradation of the adsorbed MB. Furthermore, the composite structure can offer greater surface area and porosity, improving the adsorption of MB and its subsequent exposure to photocatalytic activity. This improvement in photocatalytic efficiency not only highlights the potential of the GO/ZTO/TO composite for practical applications in the treatment of contaminated water but also addresses a crucial limitation of adsorption processes by providing a mechanism for the in situ degradation of the contaminant. The ability to degrade contaminants adsorbed directly on the adsorbent eliminates the need for the additional disposal or treatment of the contaminated adsorbent, offering a more sustainable and environmentally effective solution.

### 3.4. Reusability of GO/ZTO/TO for MB Removal

In this study, it was observed that the recovery efficiency of the GO/ZTO/TO composite is generally high and that the removal capacity of the methylene blue (MB) dye is little affected until the end of the process's fifth cycle. These results indicate that the material synthesized in this study is qualified for practical applications. The high recovery efficiency and sustained MB removal capacity after multiple use cycles reflect not only the physical and chemical stability of the GO/ZTO/TO composite but also its potential to be used in long-term applications in the treatment of sewage water. The persistence of the adsorption capacity suggests that the active sites in the composite maintain their accessibility and affinity for the MB throughout the reuse cycles, which is an indicator of the robustness of the material and the stability of the adsorbate–adsorbent interactions. These findings are especially relevant when considering the economic and environmental aspects of water treatment processes. The ability to reuse an adsorbent reduces the need to synthesize new materials for each application, which in turn not only reduces operating costs but also

decreases the environmental footprint associated with the production and disposal of adsorbents. This use and reuse cycle reflects a step towards sustainability, aligning with global efforts to minimize waste and optimize resource utilization. Furthermore, the reuse of the GO/ZTO/TO composite highlights the importance of exploring efficient regeneration methods that can restore the adsorption capacity of the material without compromising its structure or function. Future research could focus on optimizing regeneration conditions, such as the type of solvent used, desorption method, and thermal conditions, to maximize the lifetime of the materials and its cost-effectiveness in practical applications.

Finally, the efficient recovery and repeated use of the GO/ZTO/TO composite show a comprehensive approach that extends beyond the immediate utility of the composite, to encompass the broader considerations of sustainability and economic viability, which constitutes a compelling argument for its use in wastewater treatment.

## 4. Materials and Methods

### 4.1. Materials

All chemicals were used as received, without further purification: acetic acid ( $\text{CH}_3\text{COOH}$ , Sigma Aldrich, St. Louis, MO, USA, 99.8%); graphite powder ( $<150\ \mu\text{m}$ , Sigma-Aldrich, Burlington, MA, USA, 99.99%); hydrogen peroxide solution ( $\text{H}_2\text{O}_2$ , Sigma Aldrich, St. Louis, MO, USA, 30.0% in  $\text{H}_2\text{O}$ ); hydrochloric acid ( $\text{HCl}$ , Sigma Aldrich, St. Louis, MO, USA, 37.0%); isopropyl alcohol ( $\text{C}_3\text{H}_8\text{O}$ , Sigma Aldrich, St. Louis, MO, USA,  $\geq 99.5\%$ ); methanol ( $\text{CH}_3\text{OH}$ , Sigma Aldrich,  $\geq 99.8\%$ ); methylene blue (MB,  $\text{C}_{16}\text{H}_{18}\text{N}_3\text{ClS}$ , Sigma-Aldrich, Burlington, MA, USA); potassium permanganate ( $\text{KMnO}_4$ , Sigma-Aldrich, Burlington, MA, USA,  $\geq 99.0\%$ ); sodium hydroxide ( $\text{NaOH}$ , Sigma Aldrich, St. Louis, MO, USA,  $\geq 85.0\%$ ); sulfuric acid ( $\text{H}_2\text{SO}_4$ , Sigma-Aldrich, Burlington, MA, USA, 95.0–98.0%); titanium (IV) isopropoxide ( $\text{Ti}(\text{OC}_3\text{H}_7)_4$ , Sigma Aldrich, St. Louis, MO, USA, 98.0%); and zinc acetate dihydrate ( $\text{Zn}(\text{CH}_3\text{COO})_2 \cdot 2\text{H}_2\text{O}$ , ACS, St. Louis, MO, USA,  $\geq 98.0\%$ ).

### 4.2. Synthesis of GO/ZTO/TO Composite

Initially, graphene oxide (GO) synthesis was conducted via the modified Hummers method [102]. Graphite powder (3.0 g) was mixed with sulfuric acid (70 mL) under continuous agitation. Potassium permanganate (9.0 g) was gradually introduced into the mixture under mild stirring within an ice bath for 30 min. The mixture was then relocated to a 50 °C water bath, stirring persistently for another 30 min. Following this, 150 mL of distilled water was incorporated and stirred for 20 min, ensuring the temperature remained below 90 °C. Subsequently, an addition of 500 mL of distilled water and 15 mL of 30% hydrogen peroxide ensued. The mixture was allowed to settle at ambient temperature for 24 h. The sediment was centrifuged at 1000 rpm for 12 min and washed thrice with 15 mL of hydrochloric acid ( $\text{HCl}$ ) (1:10). A further centrifugation at 1000 rpm for 12 min followed, with repeated washing using distilled water until achieving a neutral pH of approximately 7. The sample was then oven-dried at 100 °C for 24 h. Post-oxidation, the sample (100 mg) was dispersed in 1 L of distilled water via sonication for 30 min and centrifuged to segregate GO from unexfoliated graphite oxide particles.

The  $\text{ZnTiO}_3/\text{TiO}_2$  (ZTO/TO) hybrid semiconductor was fabricated employing a previously established methodology [103]. Titanium isopropoxide (35 mL) was blended with isopropyl alcohol (15 mL) at 50 °C with constant stirring. Separately, zinc acetate dihydrate (8.39 g) was dissolved in water (10 mL) under agitation until fully dissolved, then mixed with isopropyl alcohol (10 mL) and maintained at 50 °C with ongoing stirring. The hybrid photocatalyst was prepared using a  $\text{ZnO}/\text{TiO}_2$  molar ratio of 1:3 by gradually adding the zinc solution to the titanium solution and continuing to stir at 50 °C until a precipitate formed. This precipitate was dried at 90 °C for 24 h and calcined at 500 °C for 4 h with a temperature increase of 2 °C/min.

For the synthesis of the GO/ZTO/TO composite, a hydrothermal method was applied [57]. Graphene oxide (GO) (100 mg) was first mixed with 40 mL of water and sonicated for 2 h. Then, 80 mL of water and 40 mL of ethanol were added to the mixture,

which underwent further sonication for 2 h to ensure thorough dispersion. Next, 500 mg of  $\text{ZnTiO}_3/\text{TiO}_2$  (ZTO/TO), synthesized via the sol-gel approach, was introduced and the solution was stirred at room temperature for 24 h. The mixture was then placed in a 300 mL autoclave reactor and heated at 100 °C and 21 psia for 24 h. The final step involved drying the resultant product in an oven at 100 °C for approximately 24 h.

#### 4.3. Characterization of GO/ZTO/TO Composite

The sample analysis was carried out utilizing the methods outlined in our earlier research [104]. X-ray diffraction (XRD) data were obtained through a Bruker-AXS D8-Discover diffractometer (Bruker AXS, Karlsruhe, Germany) equipped with Cu K $\alpha$  radiation ( $\lambda = 1.5406 \text{ \AA}$ ). Crystalline phase recognition was performed using the Crystallography Open Database (COD, version 2023). For the examination of microstructures, SEM images and EDX analyses were conducted using a JEOL JSM 6400 scanning electron microscope (SEM) (JEOL, Peabody, MA, USA), integrated with a JEOL-made dispersive X-ray spectrometer (EDS). The specific surface area (SSA) of the GO/ZTO/TO composite was measured via nitrogen adsorption at  $-196 \text{ °C}$  on a ChemiSorb 2720-unit (Micromeritics, Norcross, GA, USA), with a nitrogen (30%) and helium (70%) gas mixture. The SSA was calculated following the Brunauer-Emmett-Teller (BET) theory, applying the Chemisoft TPx software (version 1.03; Micromeritics, 2011) for the analysis based on the single-point method. The point of zero charge (PZC) for the GO/ZTO/TO composite was evaluated at ambient temperature (20 °C) by mixing 0.1 g of the composite powder in a 50 mL tube with 25 mL of 0.1 M NaCl solution, adjusting the pH to a range of 3 to 10 using 0.1 M of HCl or NaOH, and documenting the initial pH ( $\text{pH}_i$ ). After 24 h of stirring at 250 rpm, the final pH ( $\text{pH}_f$ ) was recorded. The  $\text{pH}_{\text{PZC}}$  was identified where the plot of initial versus final pH intersected with the line where initial pH equals final pH. This experiment was repeated thrice to ascertain the average  $\text{pH}_{\text{PZC}}$  for the composite [105,106]. The residual methylene blue (MB) concentration in solutions was quantified using a Jenway 7350 spectrophotometer (Cole-Parmer, Staffordshire, UK) at 623 nm.

#### 4.4. Adsorption Studies

##### aDSA

In this study, adsorption tests were performed using GO/ZTO/TO composite in methylene blue (MB) aqueous solutions to examine the influence of several variables such as pH levels, the initial concentration of adsorbate, the temperature of the reaction environment, and the duration of contact between adsorbate and adsorbent. Data from these experiments were evaluated by applying isotherm and kinetic modeling through nonlinear least-squares regression analysis [107].

The adsorptive potential of 100 mg of the GO/ZTO/TO composite was determined in MB solutions ( $10 \text{ mg L}^{-1}$ ) over a pH spectrum of 3 to 12, with the pH adjusted using 0.1 M of HCl and 0.1 M of NaOH. Solutions were mixed continuously for 24 h at room temperature before the measurement of the remaining MB concentration. Additional adsorption tests utilized a batch reactor at a stabilized pH of  $7.0 \pm 0.1$  and ambient temperature ( $20 \pm 2.0 \text{ °C}$ ), with  $200 \text{ mg L}^{-1}$  of the composite. The exploration of the composite's maximal adsorption capability involved altering MB concentrations within a 500 mL solution from 2.5 to  $50 \text{ mg L}^{-1}$ . Adsorption thermodynamics and kinetics were assessed with a  $20 \text{ mg L}^{-1}$  MB solution, using UV-visible spectrophotometry at 623 nm and a calibration curve ( $R^2 = 0.9987$ ) based on the Lambert-Beer Law. These experiments were conducted in triplicate, and the average results were documented. The calculation of the dye adsorbed by the GO/ZTO/TO composite followed Equation (2) [108], as shown in Table 1.

The study also analyzed the equilibrium adsorption of MB using the Langmuir [109], Freundlich [110], and Temkin [111] models, corresponding to Equations (3)–(5) in Table 1, respectively. The adsorption heat (B) and separation factor ( $R_L$ ) constants were determined via Equations (6) and (7) [109], shedding light on the adsorption properties.

Thermodynamic variables such as Gibbs free energy ( $\Delta G^0$ ), enthalpy change ( $\Delta H^0$ ), and entropy change ( $\Delta S^0$ ) were derived from Equation (8) [112] in Table 1. The van't Hoff equation, presented as Equation (9) in Table 1, helped establish the relationship among these parameters. The dimensionless constant  $k_C$  was computed by multiplying  $k_L$  with the adsorbate's molecular weight ( $M_w$ ) and adjusting for 1000 moles of water per liter, as explained in Equation (10) [113] in Table 1. Moreover, the kinetics of adsorption were scrutinized through various models including pseudo-first-order, pseudo-second-order, Elovich, and diffusion models (intraparticle, external film, and internal pore) [110,111], each represented by mathematical formulations (11) to (16) as listed in Table 1.

#### 4.5. Photodegradation Studies

The procedures for heterogeneous photocatalysis were adapted from previously established methods [114]. These procedures took place under UVC light exposure ( $\lambda = 254$  nm, 60 watts) using a batch setup. The pH of the solutions was regulated to  $7.0 \pm 0.1$  with the aid of 0.1 M solutions of hydrochloric acid or sodium hydroxide. In a typical experiment, semiconductor nanoparticles were agitated magnetically within a 500 mL solution of methylene blue (MB), concentrated at  $20 \text{ mg L}^{-1}$ . The reduction rate of the MB dye under UV light in these photocatalytic systems was quantitatively assessed by applying the Langmuir–Hinshelwood model [115], denoted as Equation (17) in Table 1.

#### 4.6. Reuse of GO/ZTO/TO Composite

To assess the reusability of the GO/ZTO/TO composite, it underwent desorption following a single treatment cycle [116]. Methanol was employed to release MB dye from the saturated adsorbent. Post-desorption, the adsorbent was dried and subjected to identical conditions for further use. This recycling routine was executed across three successive cycles. During each cycle, the composite was exposed to a fresh 500 mL MB solution ( $20 \text{ mg L}^{-1}$ ), with the concentration of GO/ZTO/TO kept constant at  $200 \text{ mg L}^{-1}$ .

### 5. Conclusions

This study has demonstrated the effectiveness of graphene oxide compounds in removing industrial dyes from water, underscoring their potential for practical applications in wastewater treatment. The high recovery efficiency and sustained dye removal capacity over multiple use cycles underscore the physical and chemical robustness of the GO/ZTO/TO composite, as well as its viability for long-term use. The persistence of adsorption capacity not only reflects the stability of the material but also the effectiveness of adsorbate–adsorbent interactions, indicating that the active sites of the compound maintain their accessibility and affinity for the contaminant during all reuse cycles.

The potential of adsorbent reuse points towards a sustainable and economically viable direction for the management of dye pollution in water, by reducing the need to synthesize new materials for each application and decreasing the operational costs and environmental impact associated with the adsorbent production and waste management. The importance of exploring efficient regeneration methods, which can restore the adsorption capacity of the material without compromising its structure or function, becomes evident, thereby suggesting areas for future research focused on optimizing regeneration conditions to maximize the shelf life and profitability of the material in practical applications.

Finally, the findings of this study not only validate the scientific effectiveness of graphene oxide compounds as adsorbents in removing contaminants from water but also emphasize their sustainability and economic viability. This work lays the foundation for the future development of more sustainable and cost-effective water treatment technologies, opening new avenues to address critical environmental challenges in the wastewater treatment sector.

**Author Contributions:** Conceptualization, X.J.-F.; methodology, X.J.-F. and G.C.; software, X.J.-F.; validation, X.J.-F. and G.C.; formal analysis, X.J.-F.; investigation, X.J.-F. and G.C.; resources, X.J.-F.; data curation, X.J.-F. and G.C.; writing—original draft preparation, X.J.-F. and G.C.; writing—review and editing, X.J.-F.; visualization, X.J.-F. and G.C.; supervision, X.J.-F.; project administration, X.J.-F.; funding acquisition, X.J.-F. All authors have read and agreed to the published version of the manuscript.

**Funding:** This research was funded by Universidad Técnica Particular de Loja.

**Institutional Review Board Statement:** Not applicable.

**Informed Consent Statement:** Not applicable.

**Data Availability Statement:** The data are available from the authors upon reasonable request.

**Acknowledgments:** The authors would like to thank Mónica Vega from Universidad Técnica Particular de Loja (Ecuador) and Xavier Cattoen from the Institut NEEL-CNRS (Grenoble, France) for the XRD and SEM/EDS measurements, respectively.

**Conflicts of Interest:** The authors declare no conflicts of interest.

## References

1. Carmen, Z.; Daniel, S. Textile Organic Dyes—Characteristics, Polluting Effects and Separation/Elimination Procedures from Industrial Effluents—A Critical Overview. In *Organic Pollutants Ten Years after the Stockholm Convention—Environmental and Analytical Update*; IntechOpen: London, UK, 2012; ISBN 978-953-307-917-2.
2. Ashrafi, M.; Arab Chamjangali, M.; Bagherian, G.; Goudarzi, N. Application of linear and non-linear methods for modeling removal efficiency of textile dyes from aqueous solutions using magnetic Fe<sub>3</sub>O<sub>4</sub> impregnated onto walnut shell. *Spectrochim. Acta Part A Mol. Biomol. Spectrosc.* **2017**, *171*, 268–279. [[CrossRef](#)] [[PubMed](#)]
3. Alsukaibi, A.K. Various Approaches for the Detoxification of Toxic Dyes in Wastewater. *Processes* **2022**, *10*, 1968. [[CrossRef](#)]
4. Dutta, A.K.; Ghorai, U.K.; Chattopadhyay, K.K.; Banerjee, D. Removal of textile dyes by carbon nanotubes: A comparison between adsorption and UV assisted photocatalysis. *Phys. E Low-Dimens. Syst. Nanostruct.* **2018**, *99*, 6–15. [[CrossRef](#)]
5. Samsami, S.; Mohamadi, M.; Sarrafzadeh, M.H.; Rene, E.R.; Firoozbahr, M. Recent advances in the treatment of dye-containing wastewater from textile industries: Overview and perspectives. *Process Saf. Environ. Prot.* **2020**, *143*, 138–163. [[CrossRef](#)]
6. Manappadan, Z.; Kumar, S.; Joshi, K.; Govindaraja, T.; Krishnamurthy, S.; Selvaraj, K. Unravelling the distinct surface interactions of modified graphene nanostructures with methylene blue dye through experimental and computational approaches. *J. Hazard. Mater.* **2020**, *388*, 121755. [[CrossRef](#)] [[PubMed](#)]
7. Al-Tohamy, R.; Ali, S.S.; Li, F.; Okasha, K.M.; Mahmoud, Y.A.G.; Elsamahy, T.; Jiao, H.; Fu, Y.; Sun, J. A critical review on the treatment of dye-containing wastewater: Ecotoxicological and health concerns of textile dyes and possible remediation approaches for environmental safety. *Ecotoxicol. Environ. Saf.* **2022**, *231*, 113160. [[CrossRef](#)] [[PubMed](#)]
8. Sophia, A.C.; Lima, E.C. Removal of emerging contaminants from the environment by adsorption. *Ecotoxicol. Environ. Saf.* **2018**, *150*, 1–17. [[CrossRef](#)] [[PubMed](#)]
9. Schönbacher, M.; Fehr, M.A. Basics of Ion Exchange Chromatography for Selected Geological Applications. In *Treatise on Geochemistry: Second Edition*; Elsevier: Amsterdam, The Netherlands, 2013; Volume 15, pp. 123–146, ISBN 978-0-08098-300-4.
10. Pronk, W.; Ding, A.; Morgenroth, E.; Derlon, N.; Desmond, P.; Burkhardt, M.; Wu, B.; Fane, A.G. Gravity-driven membrane filtration for water and wastewater treatment: A review. *Water Res.* **2019**, *149*, 553–565. [[CrossRef](#)] [[PubMed](#)]
11. Hu, H.; Xu, K. Physicochemical technologies for HRP and risk control. In *High-Risk Pollutants in Wastewater*; Elsevier: Amsterdam, The Netherlands, 2020; pp. 169–207. [[CrossRef](#)]
12. Martín-Pozo, L.; Del Carmen Gómez-Regalado, M.; García-Córcoles, M.T.; Zafra-Gómez, A. Removal of quinolone antibiotics from wastewaters and sewage sludge. In *Emerging Contaminants in the Environment: Challenges and Sustainable Practices*; Elsevier: Amsterdam, The Netherlands, 2022; pp. 381–406, ISBN 978-0-32385-160-2.
13. Moura, L.; Picão, R.C. Removal of antimicrobial resistance determinants from wastewater: A risk perspective on conventional and emerging technologies. In *Emerging Contaminants in the Environment: Challenges and Sustainable Practices*; Elsevier: Amsterdam, The Netherlands, 2022; pp. 603–642, ISBN 978-0-32385-160-2.
14. Ayare, S.D.; Gogate, P.R. Degradation of Tricyclazole fungicide using combined oxidation strategies based on ultrasound, ultraviolet irradiation and microwave. *Environ. Technol. Innov.* **2022**, *26*, 102533. [[CrossRef](#)]
15. Rabajczyk, A.; Zielecka, M.; Klapsa, W.; Dziechciarz, A. Self-cleaning coatings and surfaces of modern building materials for the removal of some air pollutants. *Materials* **2021**, *14*, 2161. [[CrossRef](#)]
16. Abu Hasan, H.; Muhammad, M.H.; Ismail, N.I. A review of biological drinking water treatment technologies for contaminants removal from polluted water resources. *J. Water Process Eng.* **2020**, *33*, 101035. [[CrossRef](#)]
17. Sahoo, T.R.; Prelot, B. Adsorption processes for the removal of contaminants from wastewater: The perspective role of nanomaterials and nanotechnology. In *Nanomaterials for the Detection and Removal of Wastewater Pollutants*; Elsevier: Amsterdam, The Netherlands, 2020; pp. 161–222, ISBN 978-0-12818-489-9.

18. Liu, T.; Wang, Z.; Wang, X.; Yang, G.; Liu, Y. Adsorption-photocatalysis performance of polyaniline/dicarboxyl acid cellulose@graphene oxide for dye removal. *Int. J. Biol. Macromol.* **2021**, *182*, 492–501. [[CrossRef](#)]
19. Minitha, C.R.; Lalitha, M.; Jeyachandran, Y.L.; Senthilkumar, L.; Rajendra Kumar, R.T. Adsorption behaviour of reduced graphene oxide towards cationic and anionic dyes: Co-action of electrostatic and  $\pi$ - $\pi$  interactions. *Mater. Chem. Phys.* **2017**, *194*, 243–252. [[CrossRef](#)]
20. Upadhyay, G.K.; Rajput, J.K.; Pathak, T.K.; Kumar, V.; Purohit, L.P. Synthesis of ZnO:TiO<sub>2</sub> nanocomposites for photocatalyst application in visible light. *Vacuum* **2019**, *160*, 154–163. [[CrossRef](#)]
21. Amaro-Medina, B.M.; Martinez-Luevanos, A.; Soria-Aguilar, M.; Sanchez-Castillo, M.A.; Estrada-Flores, S.; Carrillo-Pedroza, F.R. Efficiency of Adsorption and Photodegradation of Composite TiO<sub>2</sub>/Fe<sub>2</sub>O<sub>3</sub> and Industrial Wastes in Cyanide Removal. *Water* **2022**, *14*, 3502. [[CrossRef](#)]
22. Muthirulan, P.; Nirmala Devi, C.; Meenakshi Sundaram, M. Synchronous role of coupled adsorption and photocatalytic degradation on CAC-TiO<sub>2</sub> composite generating excellent mineralization of alizarin cyanine green dye in aqueous solution. *Arab. J. Chem.* **2017**, *10*, S1477–S1483. [[CrossRef](#)]
23. Rout, D.R.; Jena, H.M.; Baigenzhenov, O.; Hosseini-Bandegharai, A. Graphene-based materials for effective adsorption of organic and inorganic pollutants: A critical and comprehensive review. *Sci. Total Environ.* **2023**, *863*, 160871. [[CrossRef](#)] [[PubMed](#)]
24. Wang, J.; Wang, S. Reactive species in advanced oxidation processes: Formation, identification and reaction mechanism. *Chem. Eng. J.* **2020**, *401*, 126158. [[CrossRef](#)]
25. Nissanka, B.; Kottegoda, N.; Jayasundara, D.R. Probing structural variations of graphene oxide and reduced graphene oxide using methylene blue adsorption method. *J. Mater. Sci.* **2020**, *55*, 1996–2005. [[CrossRef](#)]
26. Wang, H.; Yi, L.; Huang, F.; Huang, Q.; Zhou, T. Facile synthesis of graphene nanosheets on wastewater sediments for high efficient adsorption of methylene blue. *Sep. Purif. Technol.* **2024**, *337*, 126366. [[CrossRef](#)]
27. Ben Gouider Trabelsi, A.; Kusmartsev, F.V.; Kusmartseva, A.; Alkallas, F.H.; Alfaiy, S.; Shkir, M. Raman Spectroscopy Imaging of Exceptional Electronic Properties in Epitaxial Graphene Grown on SiC. *Nanomaterials* **2020**, *10*, 2234. [[CrossRef](#)] [[PubMed](#)]
28. Baig, N.; Ihsanullah; Sajid, M.; Saleh, T.A. Graphene-based adsorbents for the removal of toxic organic pollutants: A review. *J. Environ. Manag.* **2019**, *244*, 370–382. [[CrossRef](#)] [[PubMed](#)]
29. Rivera Tito, H.A.; Hernandez-Sosa, G.; Cucinotta, F.; Huang, X.; Quintana Caceda, M.E. Photoluminescent graphene oxide porous particles in solution under environmental conditions produced by hydrothermal treatment. *Mater. Today Commun.* **2019**, *20*, 100621. [[CrossRef](#)]
30. Gascho, J.L.S.; Costa, S.F.; Recco, A.A.C.; Pezzin, S.H. Graphene oxide films obtained by vacuum filtration: X-ray diffraction evidence of crystalline reorganization. *J. Nanomater.* **2019**, *2019*, 5963148. [[CrossRef](#)]
31. Fraga, T.J.M.; Carvalho, M.N.; Ghislandi, M.G.; Da Motta Sobrinho, M.A. Functionalized graphene-based materials as innovative adsorbents of organic pollutants: A concise overview. *Braz. J. Chem. Eng.* **2019**, *36*, 1–31. [[CrossRef](#)]
32. Esteban-Arranz, A.; Compte-Tordesillas, D.; Muñoz-Andrés, V.; Pérez-Cadenas, M.; Guerrero-Ruiz, A. Effect of surface, structural and textural properties of graphenic materials over cooperative and synergetic adsorptions of two chloroaromatic compounds from aqueous solution. *Catal. Today* **2018**, *301*, 104–111. [[CrossRef](#)]
33. Vacchi, I.A.; Ménard-Moyon, C.; Bianco, A. Chemical Functionalization of Graphene Family Members. *Phys. Sci. Rev.* **2017**, *2*, 20160103. [[CrossRef](#)]
34. Dreyer, D.R.; Murali, S.; Zhu, Y.; Ruoff, R.S.; Bielawski, C.W. Reduction of graphite oxide using alcohols. *J. Mater. Chem.* **2011**, *21*, 3443–3447. [[CrossRef](#)]
35. Luo, D.; Zhang, G.; Liu, J.; Sun, X. Evaluation criteria for reduced graphene oxide. *J. Phys. Chem. C* **2011**, *115*, 11327–11335. [[CrossRef](#)]
36. Rao, C.N.R.; Gopalakrishnan, K.; Govindaraj, A. Synthesis, properties and applications of graphene doped with boron, nitrogen and other elements. *Nano Today* **2014**, *9*, 324–343. [[CrossRef](#)]
37. Xue, Y.; Wu, B.; Bao, Q.; Liu, Y. Controllable Synthesis of Doped Graphene and Its Applications. *Small* **2014**, *10*, 2975–2991. [[CrossRef](#)]
38. Chang, H.; Wu, H. Graphene-based nanocomposites: Preparation, functionalization, and energy and environmental applications. *Energy Environ. Sci.* **2013**, *6*, 3483–3507. [[CrossRef](#)]
39. Luo, J.; Luo, X.; Gan, Y.; Xu, X.; Xu, B.; Liu, Z.; Ding, C.; Cui, Y.; Sun, C. Advantages of Bimetallic Organic Frameworks in the Adsorption, Catalysis and Detection for Water Contaminants. *Nanomaterials* **2023**, *13*, 2194. [[CrossRef](#)] [[PubMed](#)]
40. Ramesha, G.K.; Vijaya Kumara, A.; Muralidhara, H.B.; Sampath, S. Graphene and graphene oxide as effective adsorbents toward anionic and cationic dyes. *J. Colloid Interface Sci.* **2011**, *361*, 270–277. [[CrossRef](#)] [[PubMed](#)]
41. Justino, D.D.; Alves, M.O.; Galvão, B.R.L.; Santamaría, R.; De Sousa, F.B.; Ortega, P.F.R. The effects of functionalization on graphene oxide for organic dye adsorption: An experimental-theoretical study using electronic structure calculations and statistical mechanical modeling. *J. Mol. Liq.* **2023**, *387*, 122612. [[CrossRef](#)]
42. Dayana Priyadharshini, S.; Manikandan, S.; Kiruthiga, R.; Rednam, U.; Babu, P.S.; Subbaiya, R.; Karmegam, N.; Kim, W.; Govarthanam, M. Graphene oxide-based nanomaterials for the treatment of pollutants in the aquatic environment: Recent trends and perspectives—A review. *Environ. Pollut.* **2022**, *306*, 119377. [[CrossRef](#)] [[PubMed](#)]
43. Mandeep; Gulati, A.; Kakkar, R. Graphene-based adsorbents for water remediation by removal of organic pollutants: Theoretical and experimental insights. *Chem. Eng. Res. Des.* **2020**, *153*, 21–36. [[CrossRef](#)]

44. Fraga, T.J.M.; Ghislandi, M.G.; Carvalho, M.N.; da Motta Sobrinho, M.A. One step forward: How can functionalization enhance the adsorptive properties of graphene towards metallic ions and dyes? *Environ. Res.* **2020**, *184*, 109362. [[CrossRef](#)] [[PubMed](#)]
45. Tee, W.T.; Loh, N.Y.L.; Lai, K.C.; Hiew, B.Y.Z.; Gan, S.; Lee, L.Y. Application of 3D heteroatom-doped graphene in adsorptive removal of water pollutants: Review on hydrothermal synthesis and its influencing factors. *Sep. Purif. Technol.* **2023**, *320*, 124072. [[CrossRef](#)]
46. Zhu, B.; Yang, Q.; Zhang, W.; Cui, S.; Yang, B.; Wang, Q.; Li, S.; Zhang, D. A high sensitivity dual-mode optical thermometry based on charge compensation in ZnTiO<sub>3</sub>:M (M = Eu<sup>3+</sup>, Mn<sup>4+</sup>) hexagonal prisms. *Spectrochim. Acta Part A Mol. Biomol. Spectrosc.* **2022**, *274*, 121101. [[CrossRef](#)] [[PubMed](#)]
47. Mofokeng, S.J.; Noto, L.L.; Dhlamini, M.S. Photoluminescence properties of ZnTiO<sub>3</sub>:Eu<sup>3+</sup> phosphor with enhanced red emission by Al<sup>3+</sup> charge compensation. *J. Lumin.* **2020**, *228*, 117569. [[CrossRef](#)]
48. Zhang, J.; Xu, B.; Wang, Y.S.; Qin, Z.; Ke, S.H. First-principles investigation of the ferroelectric, piezoelectric and nonlinear optical properties of LiNbO<sub>3</sub>-type ZnTiO<sub>3</sub>. *Sci. Rep.* **2019**, *9*, 17632. [[CrossRef](#)] [[PubMed](#)]
49. Djellabi, R.; Ordonez, M.F.; Conte, F.; Falletta, E.; Bianchi, C.L.; Rossetti, I. A Review of Advances in Multifunctional XTiO<sub>3</sub> Perovskite-type Oxides as piezo-photocatalysts for Environmental Remediation and Energy Production. *J. Hazard. Mater.* **2021**, *421*, 126792. [[CrossRef](#)] [[PubMed](#)]
50. Bhagwat, U.O.; Wu, J.J.; Asiri, A.M.; Anandan, S. Synthesis of ZnTiO<sub>3</sub>@TiO<sub>2</sub> Heterostructure Nanomaterial as a Visible light Photocatalyst. *ChemistrySelect* **2019**, *4*, 6106–6112. [[CrossRef](#)]
51. Jaramillo-Fierro, X.; Hernández, K.; González, S. Cu(C<sub>3</sub>H<sub>3</sub>N<sub>3</sub>S<sub>3</sub>)<sub>3</sub> Adsorption onto ZnTiO<sub>3</sub>/TiO<sub>2</sub> for Coordination-Complex Sensitized Photochemical Applications. *Materials* **2022**, *15*, 3252. [[CrossRef](#)] [[PubMed](#)]
52. Mohamadi Zalani, N.; Koozegar Kaleji, B.; Mazinani, B. Synthesis and characterisation of the mesoporous ZnO-TiO<sub>2</sub> nanocomposite; Taguchi optimisation and photocatalytic methylene blue degradation under visible light. *Mater. Technol.* **2020**, *35*, 281–289. [[CrossRef](#)]
53. Jose, M.; Elakiya, M.; Dhas, S.A.M.B. Structural and optical properties of nanosized ZnO/ZnTiO<sub>3</sub> composite materials synthesized by a facile hydrothermal technique. *J. Mater. Sci. Mater. Electron.* **2017**, *28*, 13649–13658. [[CrossRef](#)]
54. Chen, F.; Yu, C.; Wei, L.; Fan, Q.; Ma, F.; Zeng, J.; Yi, J.; Yang, K.; Ji, H. Fabrication and characterization of ZnTiO<sub>3</sub>/Zn<sub>2</sub>Ti<sub>3</sub>O<sub>8</sub>/ZnO ternary photocatalyst for synergetic removal of aqueous organic pollutants and Cr(VI) ions. *Sci. Total Environ.* **2020**, *706*, 136026. [[CrossRef](#)] [[PubMed](#)]
55. Arabpour, A.; Dan, S.; Hashemipour, H. Preparation and optimization of novel graphene oxide and adsorption isotherm study of methylene blue. *Arab. J. Chem.* **2021**, *14*, 103003. [[CrossRef](#)]
56. Yan, H.; Tao, X.; Yang, Z.; Li, K.; Yang, H.; Li, A.; Cheng, R. Effects of the oxidation degree of graphene oxide on the adsorption of methylene blue. *J. Hazard. Mater.* **2014**, *268*, 191–198. [[CrossRef](#)] [[PubMed](#)]
57. Kang, C.; Xiao, K.; Yao, Z.; Wang, Y.; Huang, D.; Zhu, L.; Liu, F.; Tian, T. Hydrothermal synthesis of graphene-ZnTiO<sub>3</sub> nanocomposites with enhanced photocatalytic activities. *Res. Chem. Intermed.* **2018**, *44*, 6621–6636. [[CrossRef](#)]
58. Holzwarth, U.; Gibson, N. The Scherrer equation versus the “Debye-Scherrer equation”. *Nat. Nanotechnol.* **2011**, *6*, 534. [[CrossRef](#)] [[PubMed](#)]
59. Emiru, T.F.; Ayele, D.W. Controlled synthesis, characterization and reduction of graphene oxide: A convenient method for large scale production. *Egypt. J. Basic Appl. Sci.* **2017**, *4*, 74–79. [[CrossRef](#)]
60. Mehrabi, M.; Javanbakht, V. Photocatalytic degradation of cationic and anionic dyes by a novel nanophotocatalyst of TiO<sub>2</sub>/ZnTiO<sub>3</sub>/αFe<sub>2</sub>O<sub>3</sub> by ultraviolet light irradiation. *J. Mater. Sci. Mater. Electron.* **2018**, *29*, 9908–9919. [[CrossRef](#)]
61. Tahay, P.; Khani, Y.; Jabari, M.; Bahadoran, F.; Safari, N.; Zamanian, A. Synthesis of cubic and hexagonal ZnTiO<sub>3</sub> as catalyst support in steam reforming of methanol: Study of physical and chemical properties of copper catalysts on the H<sub>2</sub> and CO selectivity and coke formation. *Int. J. Hydrogen Energy* **2020**, *45*, 9484–9495. [[CrossRef](#)]
62. Gabal, M.A.; Angari, Y.M.A. Zinc titanates nanopowders: Synthesis and characterization. *Mater. Res. Express* **2022**, *9*, 025010. [[CrossRef](#)]
63. Ramakrishnan, V.M.; Natarajan, M.; Santhanam, A.; Asokan, V.; Velauthapillai, D. Size controlled synthesis of TiO<sub>2</sub> nanoparticles by modified solvothermal method towards effective photo catalytic and photovoltaic applications. *Mater. Res. Bull.* **2018**, *97*, 351–360. [[CrossRef](#)]
64. Tene, T.; Guevara, M.; Valarezo, A.; Salguero, O.; Arias Arias, F.; Arias, M.; Scarcello, A.; Caputi, L.S.; Vacacela Gomez, C. Drying-time study in graphene oxide. *Nanomaterials* **2021**, *11*, 1035. [[CrossRef](#)] [[PubMed](#)]
65. Rueden, C.T.; Schindelin, J.; Hiner, M.C.; DeZonia, B.E.; Walter, A.E.; Arena, E.T.; Eliceiri, K.W. ImageJ2: ImageJ for the next generation of scientific image data. *BMC Bioinform.* **2017**, *18*, 529. [[CrossRef](#)] [[PubMed](#)]
66. Schneider, C.A.; Rasband, W.S.; Eliceiri, K.W. NIH Image to ImageJ: 25 years of image analysis. *Nat. Methods* **2012**, *9*, 671–675. [[CrossRef](#)] [[PubMed](#)]
67. Tran, D.T.; Nguyen, V.N. RGO/persulfate metal-free catalytic system for the degradation of tetracycline: Effect of reaction parameters. *Mater. Res. Express* **2020**, *7*, 075501. [[CrossRef](#)]
68. Chaabane, L.; Beyou, E.; Luneau, D.; Baouab, M.H.V. Functionalization of graphene oxide sheets with magnetite nanoparticles for the adsorption of copper ions and investigation of its potential catalytic activity toward the homocoupling of alkynes under green conditions. *J. Catal.* **2020**, *388*, 91–103. [[CrossRef](#)]

69. Tavakoli-Azar, T.; Mahjoub, A.R.; Sadjadi, M.S.; Farhadyar, N.; Sadr, M.H. Improving the photocatalytic performance of a perovskite ZnTiO<sub>3</sub> through ZnTiO<sub>3</sub>@S nanocomposites for degradation of Crystal violet and Rhodamine B pollutants under sunlight. *Inorg. Chem. Commun.* **2020**, *119*, 108091. [[CrossRef](#)]
70. Kunnamareddy, M.; Diravidamani, B.; Rajendran, R.; Singaram, B.; Varadharajan, K. Synthesis of silver and sulphur codoped TiO<sub>2</sub> nanoparticles for photocatalytic degradation of methylene blue. *J. Mater. Sci. Mater. Electron.* **2018**, *29*, 18111–18119. [[CrossRef](#)]
71. Jahan, N.; Roy, H.; Reaz, A.H.; Arshi, S.; Rahman, E.; Firoz, S.H.; Islam, M.S. A comparative study on sorption behavior of graphene oxide and reduced graphene oxide towards methylene blue. *Case Stud. Chem. Environ. Eng.* **2022**, *6*, 100239. [[CrossRef](#)]
72. Dan, S.; Bagheri, H.; Shahidzadeh, A.; Hashemipour, H. Performance of graphene Oxide/SiO<sub>2</sub> Nanocomposite-based: Antibacterial Activity, dye and heavy metal removal. *Arab. J. Chem.* **2023**, *16*, 104450. [[CrossRef](#)]
73. Batzias, F.A.; Sidiras, D.K. Simulation of dye adsorption by beech sawdust as affected by pH. *J. Hazard. Mater.* **2007**, *141*, 668–679. [[CrossRef](#)] [[PubMed](#)]
74. Soltani, A.; Faramarzi, M.; Parsa, S.A.M. A review on adsorbent parameters for removal of dye products from industrial wastewater. *Water Qual. Res. J.* **2021**, *56*, 181–193. [[CrossRef](#)]
75. Gao, Y.; Ren, X.; Tan, X.; Hayat, T.; Alsaedi, A.; Chen, C. Insights into key factors controlling GO stability in natural surface waters. *J. Hazard. Mater.* **2017**, *335*, 56–65. [[CrossRef](#)] [[PubMed](#)]
76. Khatib, K.; Lahmyed, L.; El Azhari, M. Synthesis, Characterization, and Application of Geopolymer/TiO<sub>2</sub> Nanoparticles Composite for Efficient Removal of Cu(II) and Cd(II) Ions from Aqueous Media. *Minerals* **2022**, *12*, 1445. [[CrossRef](#)]
77. Bhunia, K.; Chandra, M.; Kumar Sharma, S.; Pradhan, D.; Kim, S.J. A critical review on transition metal phosphide based catalyst for electrochemical hydrogen evolution reaction: Gibbs free energy, composition, stability, and true identity of active site. *Coord. Chem. Rev.* **2023**, *478*, 214956. [[CrossRef](#)]
78. De Araujo, C.M.B.; De Assis Filho, R.B.; Baptisttella, A.M.S.; Do Nascimento, G.F.O.; Da Costa, G.R.B.; Carvalho, M.N.; Ghislandi, M.G.; Sobrinho, M.A.D.M. Systematic study of graphene oxide production using factorial design techniques and its application to the adsorptive removal of methylene blue dye in aqueous medium. *Mater. Res. Express* **2018**, *5*, 065042. [[CrossRef](#)]
79. Chen, L.; Zhu, Y.; Cui, Y.; Dai, R.; Shan, Z.; Chen, H. Fabrication of starch-based high-performance adsorptive hydrogels using a novel effective pretreatment and adsorption for cationic methylene blue dye: Behavior and mechanism. *Chem. Eng. J.* **2021**, *405*, 126953. [[CrossRef](#)]
80. Salazar-Rabago, J.J.; Leyva-Ramos, R.; Rivera-Utrilla, J.; Ocampo-Perez, R.; Cerino-Cordova, F.J. Biosorption mechanism of Methylene Blue from aqueous solution onto White Pine (*Pinus durangensis*) sawdust: Effect of operating conditions. *Sustain. Environ. Res.* **2017**, *27*, 32–40. [[CrossRef](#)]
81. Chowdhury, I.; Duch, M.C.; Mansukhani, N.D.; Hersam, M.C.; Bouchard, D. Colloidal properties and stability of graphene oxide nanomaterials in the aquatic environment. *Environ. Sci. Technol.* **2013**, *47*, 6288–6296. [[CrossRef](#)] [[PubMed](#)]
82. Hua, Z.; Tang, Z.; Bai, X.; Zhang, J.; Yu, L.; Cheng, H. Aggregation and resuspension of graphene oxide in simulated natural surface aquatic environments. *Environ. Pollut.* **2015**, *205*, 161–169. [[CrossRef](#)] [[PubMed](#)]
83. Fan, S.; Tang, J.; Wang, Y.; Li, H.; Zhang, H.; Tang, J.; Wang, Z.; Li, X. Biochar prepared from co-pyrolysis of municipal sewage sludge and tea waste for the adsorption of methylene blue from aqueous solutions: Kinetics, isotherm, thermodynamic and mechanism. *J. Mol. Liq.* **2016**, *220*, 432–441. [[CrossRef](#)]
84. Badeenezhad, A.; Azhdarpoor, A.; Bahrami, S.; Yousefinejad, S. Removal of methylene blue dye from aqueous solutions by natural clinoptilolite and clinoptilolite modified by iron oxide nanoparticles. *Mol. Simul.* **2019**, *45*, 564–571. [[CrossRef](#)]
85. An, F.; Liu, J.; Xu, Z.; Zheng, S. Efficient removal of three dyes using porous covalent triazine frameworks: Adsorption mechanism and role of pore distribution. *Water Sci. Technol.* **2020**, *82*, 3023–3031. [[CrossRef](#)] [[PubMed](#)]
86. Wang, G.; Li, G.; Huan, Y.; Hao, C.; Chen, W. Acrylic acid functionalized graphene oxide: High-efficient removal of cationic dyes from wastewater and exploration on adsorption mechanism. *Chemosphere* **2020**, *261*, 127736. [[CrossRef](#)] [[PubMed](#)]
87. Arias, F.A.; Guevara, M.; Tene, T.; Angamarca, P.; Molina, R.; Valarezo, A.; Salguero, O.; Gomez, C.V.; Arias, M.; Caputi, L.S. The adsorption of methylene blue on eco-friendly reduced graphene oxide. *Nanomaterials* **2020**, *10*, 681. [[CrossRef](#)]
88. Ai, L.; Zhang, C.; Liao, F.; Wang, Y.; Li, M.; Meng, L.; Jiang, J. Removal of methylene blue from aqueous solution with magnetite loaded multi-wall carbon nanotube: Kinetic, isotherm and mechanism analysis. *J. Hazard. Mater.* **2011**, *198*, 282–290. [[CrossRef](#)] [[PubMed](#)]
89. Mercante, L.A.; Facure, M.H.M.; Locilento, D.A.; Sanfelice, R.C.; Migliorini, F.L.; Mattoso, L.H.C.; Correa, D.S. Solution blow spun PMMA nanofibers wrapped with reduced graphene oxide as an efficient dye adsorbent. *New J. Chem.* **2017**, *41*, 9087–9094. [[CrossRef](#)]
90. Yang, M.; Liu, X.; Qi, Y.; Sun, W.; Men, Y. Preparation of κ-carrageenan/graphene oxide gel beads and their efficient adsorption for methylene blue. *J. Colloid Interface Sci.* **2017**, *506*, 669–677. [[CrossRef](#)] [[PubMed](#)]
91. Chen, J.; Jiang, M.; Han, J.; Liu, K.; Liu, M.; Wu, Q. Syntheses of magnetic GO @ melamine formaldehyde resin for dyes adsorption. *Mater. Res. Express* **2019**, *6*, 086103. [[CrossRef](#)]
92. Wang, Z.; Gao, M.; Li, X.; Ning, J.; Zhou, Z.; Li, G. Efficient adsorption of methylene blue from aqueous solution by graphene oxide modified persimmon tannins. *Mater. Sci. Eng. C* **2020**, *108*, 110196. [[CrossRef](#)] [[PubMed](#)]
93. Li, Y.; Du, Q.; Liu, T.; Sun, J.; Wang, Y.; Wu, S.; Wang, Z.; Xia, Y.; Xia, L. Methylene blue adsorption on graphene oxide/calcium alginate composites. *Carbohydr. Polym.* **2013**, *95*, 501–507. [[CrossRef](#)] [[PubMed](#)]

94. Ai, L.; Jiang, J. Removal of methylene blue from aqueous solution with self-assembled cylindrical graphene-carbon nanotube hybrid. *Chem. Eng. J.* **2012**, *192*, 156–163. [[CrossRef](#)]
95. Ai, L.; Zhang, C.; Chen, Z. Removal of methylene blue from aqueous solution by a solvothermal-synthesized graphene/magnetite composite. *J. Hazard. Mater.* **2011**, *192*, 1515–1524. [[CrossRef](#)] [[PubMed](#)]
96. Pourzare, K.; Farhadi, S.; Mansourpanah, Y. Graphene oxide/CO<sub>3</sub>O<sub>4</sub> nanocomposite: Synthesis, characterization, and its adsorption capacity for the removal of organic dye pollutants from water. *Acta Chim. Slov.* **2017**, *64*, 945–958. [[CrossRef](#)] [[PubMed](#)]
97. Guo, T.; Bulin, C. Facile fabrication of MgO/graphene oxide composite as an efficient adsorbent for rapid removal of aqueous organic dyes: Performance evaluation and mechanistic investigation. *J. Phys. Chem. Solids* **2021**, *158*, 110251. [[CrossRef](#)]
98. Tran, H.V.; Bui, L.T.; Dinh, T.T.; Le, D.H.; Huynh, C.D.; Trinh, A.X. Graphene oxide/Fe<sub>3</sub>O<sub>4</sub>/chitosan nanocomposite: A recoverable and recyclable adsorbent for organic dyes removal. Application to methylene blue. *Mater. Res. Express* **2017**, *4*, 035701. [[CrossRef](#)]
99. Allouss, D.; Essamlali, Y.; Amadine, O.; Chakir, A.; Zahouily, M. Response surface methodology for optimization of methylene blue adsorption onto carboxymethyl cellulose-based hydrogel beads: Adsorption kinetics, isotherm, thermodynamics and reusability studies. *RSC Adv.* **2019**, *9*, 37858–37869. [[CrossRef](#)] [[PubMed](#)]
100. Chavda, V.; Patel, B.; Singh, S.; Hirpara, D.; Rajeswari, V.D.; Kumar, S. A sustainable approach for the adsorption of methylene blue from an aqueous background: An adsorbent based on DES/CGS modified GO@ZrO<sub>2</sub>. *RSC Sustain.* **2023**, *1*, 2038–2057. [[CrossRef](#)]
101. Li, H.; Li, T.; Zhang, T.; Zhu, J.; Deng, W.; He, D. Construction and Adsorption Performance Study of GO-CNT/Activated Carbon Composites for High Efficient Adsorption of Pollutants in Wastewater. *Polymers* **2022**, *14*, 4951. [[CrossRef](#)] [[PubMed](#)]
102. Tene, T.; Usca, G.T.; Guevara, M.; Molina, R.; Veltri, F.; Arias, M.; Caputi, L.S.; Gomez, C.V. Toward large-scale production of oxidized graphene. *Nanomaterials* **2020**, *10*, 279. [[CrossRef](#)] [[PubMed](#)]
103. Jaramillo-Fierro, X.; Cuenca, M.F. Novel Semiconductor Cu(C<sub>3</sub>H<sub>3</sub>N<sub>3</sub>S<sub>3</sub>)<sub>3</sub>/ZnTiO<sub>3</sub>/TiO<sub>2</sub> for the Photoinactivation of *E. coli* and *S. aureus* under Solar Light. *Nanomaterials* **2023**, *13*, 173. [[CrossRef](#)] [[PubMed](#)]
104. Jaramillo-Fierro, X.; Ramón, J.; Valarezo, E. Cyanide Removal by ZnTiO<sub>3</sub>/TiO<sub>2</sub>/H<sub>2</sub>O<sub>2</sub>/UVB System: A Theoretical-Experimental Approach. *Int. J. Mol. Sci.* **2023**, *24*, 16446. [[CrossRef](#)] [[PubMed](#)]
105. Lamaiphan, N.; Sakaew, C.; Sricharoen, P.; Nuengmatcha, P.; Chanthai, S.; Limchoowong, N. Highly efficient ultrasonic-assisted preconcentration of trace amounts of Ag(I), Pb(II), and Cd(II) ions using 3-mercaptopropyl trimethoxysilane-functionalized graphene oxide–magnetic nanoparticles. *J. Korean Ceram. Soc.* **2021**, *58*, 314–329. [[CrossRef](#)]
106. Bakatula, E.N.; Richard, D.; Neculita, C.M.; Zagury, G.J. Determination of point of zero charge of natural organic materials. *Environ. Sci. Pollut. Res.* **2018**, *25*, 7823–7833. [[CrossRef](#)] [[PubMed](#)]
107. Benmessaoud, A.; Nibou, D.; Mekatel, E.H.; Amokrane, S. A Comparative Study of the Linear and Non-Linear Methods for Determination of the Optimum Equilibrium Isotherm for Adsorption of Pb<sup>2+</sup> Ions onto Algerian Treated Clay. *Iran. J. Chem. Chem. Eng.* **2020**, *39*, 153–171. [[CrossRef](#)]
108. Eke-emezie, N.; Etuk, B.R.; Akpan, O.P.; Chinweoke, O.C. Cyanide removal from cassava wastewater onto H<sub>3</sub>PO<sub>4</sub> activated periwinkle shell carbon. *Appl. Water Sci.* **2022**, *12*, 157. [[CrossRef](#)]
109. Pirmoradi, M.; Hashemian, S.; Shayesteh, M.R. Kinetics and thermodynamics of cyanide removal by ZnO@NiO nanocrystals. *Trans. Nonferrous Met. Soc. China* **2017**, *27*, 1394–1403. [[CrossRef](#)]
110. Noroozi, R.; Al-Musawi, T.J.; Kazemian, H.; Kalhori, E.M.; Zarrabi, M. Removal of cyanide using surface-modified Linde Type-A zeolite nanoparticles as an efficient and eco-friendly material. *J. Water Process Eng.* **2018**, *21*, 44–51. [[CrossRef](#)]
111. Inyinbor, A.A.; Adekola, F.A.; Olatunji, G.A. Kinetics, isotherms and thermodynamic modeling of liquid phase adsorption of Rhodamine B dye onto *Raphia hookeri* fruit epicarp. *Water Resour. Ind.* **2016**, *15*, 14–27. [[CrossRef](#)]
112. Tran, H.N.; You, S.J.; Hosseini-Bandegharaei, A.; Chao, H.P. Mistakes and inconsistencies regarding adsorption of contaminants from aqueous solutions: A critical review. *Water Res.* **2017**, *120*, 88–116. [[CrossRef](#)] [[PubMed](#)]
113. Zhou, X.; Zhou, X. The Unit Problem in the Thermodynamic Calculation of Adsorption Using the Langmuir Equation. *Chem. Eng. Commun.* **2014**, *201*, 1459–1467. [[CrossRef](#)]
114. Jaramillo-Fierro, X.; González, S.; Medina, F. La-doped ZnTiO<sub>3</sub>/TiO<sub>2</sub> nanocomposite supported on ecuadorian diatomaceous earth as a highly efficient photocatalyst driven by solar light. *Molecules* **2021**, *26*, 6232. [[CrossRef](#)] [[PubMed](#)]
115. Bettoni, M.; Falcinelli, S.; Rol, C.; Rosi, M.; Sebastiani, G.V. Gas-Phase TiO<sub>2</sub> Photosensitized Mineralization of Some VOCs: Mechanistic Suggestions through a Langmuir–Hinshelwood Kinetic Approach. *Catalysts* **2020**, *11*, 20. [[CrossRef](#)]
116. Jaramillo-Fierro, X.; González, S.; Montesdeoca-Mendoza, F.; Medina, F. Structuring of ZnTiO<sub>3</sub>/TiO<sub>2</sub> adsorbents for the removal of methylene blue, using zeolite precursor clays as natural additives. *Nanomaterials* **2021**, *11*, 898. [[CrossRef](#)] [[PubMed](#)]

**Disclaimer/Publisher’s Note:** The statements, opinions and data contained in all publications are solely those of the individual author(s) and contributor(s) and not of MDPI and/or the editor(s). MDPI and/or the editor(s) disclaim responsibility for any injury to people or property resulting from any ideas, methods, instructions or products referred to in the content.